การปลูกผลึกด้วยลำโมเลกุลของแกลเลียมอาร์เซไนด์บนแผ่นฐานเจอร์มาเนียม

เพื่อประยุกต์ใช้งานกับสิ่งประดิษฐ์ทางแสงในอนาคต

นายวิชิต   ตันติวีระโสภณ

วิทยานิพนธ์นี้เป็นส่วนหนึ่งของการศึกษาตามหลักสูตรปริญญาวิศวกรรมศาสตรมหาบัณฑิต
สาขาวิชาวิศวกรรมไฟฟ้า   ภาควิชาวิศวกรรมไฟฟ้า
คณะวิศกรรมศาสตร์ จุฬาลงกรณ์มหาวิทยาลัย
ปีการศึกษา 2553

MOLECULAR BEAM EPITAXIAL GROWTH OF GaAs ON Ge SUBSTRATES
FOR FUTURE PHOTONIC DEVICE APPLICATION

Mr. Wichit Tantiweerasophon

A Thesis Submitted in Partial Fulfillment of the Requirements
for the Degree of Master of Engineering Program in Electrical Engineering
Department of Electrical Engineering
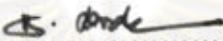Faculty of Engineering
Chulalongkorn University
Academic year 2010

Thesis Title   Molecular Beam Epitaxial Growth of GaAs on Ge Substrates for
Future Photonic Device Application
By   Mr. Wichit Tantiweerasophon
Field of Study   Electrical Engineering
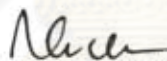Thesis Advisor   Professor Dr. Somsak Panyakeow

---

Accepted by the Faculty of Engineering, Chulalongkorn University in Partial Fulfillment of the Requirements for the Master's Degree
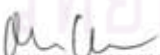
......................................Dean of Faculty of Engineering

(Associate Professor Boonsom Lerdhirunwong, Dr.Ing.)

THESIS COMMITTEE

......................................Chairman

(Associate Professor Banyong Toprasertpong, Dr.Ing.)

......................................Thesis Advisor

(Professor Somsak Panyakeow, D.Eng.)

......................................Examiner

(Associate Professor Somchai Ratanathammaphan, D.Eng)

......................................External Examiner

(Noppadon Nuntawong, Ph.D.)

......................................External Examiner

(Suwat Sopitpan, Ph.D.)

วิชิต ตันติวีระโสภณ : การปลูกผลึกด้วยลำโมเลกุลของแกลเลียมอาร์เซไนด์บนแผ่นฐานเจอร์มาเนียม เพื่อประยุกต์ใช้งานกับสิ่งประดิษฐ์ทางแสงในอนาคต. (MOLECULAR BEAM EPITAXIAL GROWTH OF GaAs ON Ge SUBSTRATES FOR FUTURE PHOTONIC DEVICE APPLICATION) อ. ที่ปรึกษาวิทยานิพนธ์หลัก : ศ.ดร. สมศักดิ์ ปัญญาแก้ว, 78 หน้า.

วิทยานิพนธ์ฉบับนี้ นำเสนอการปลูกผลึกอิพิแทกซีด้วยลำโมเลกุลของแกลเลียมอาร์เซไนด์บนแผ่นฐาน เจอร์มาเนียม แกลเลียมอาร์เซไนด์และเจอร์มาเนียมมีค่าคงตัวผลึกเท่ากัน อย่างไรก็ตามแกลเลียมอาร์เซไนด์เป็นสารกึ่ง ตัวนำมีขั้ว ในขณะที่เจอร์มาเนียมเป็นสารกึ่งตัวนำไม่มีขั้ว เมื่อแกลเลียมอาร์เซไนด์ถูกปลูกบนแผ่นฐานเจอร์มาเนียมทำ ให้เกิดแอนไทเฟสโดเมน (Anti-phase domains) ซึ่งงานวิจัยนี้ได้ทำการศึกษาสภาวะในการปลูกที่ทำให้เกิด โดเมนของแกลเลียมอาร์เซไนด์ที่มีขนาดใหญ่ โดยวิธีหลักที่ใช้ในการปลูกผลึกคือวิธีไมเกรชัน-เอนฮานซ์อิพิแทซี (Migration-enhanced epitaxy) นอกจากนี้เรายังได้ทำการปลูกอินเดียมอาร์เซไนด์ควอนตัมดอตบนแอนไท เฟสโดเมนของแกลเลียมอาร์เซไนด์เพื่อศึกษาการจัดเรียงตัวของควอนตัมดอต โดยพบว่าดอตจะเรียงตัวในทิศทางที่ แน่นอนในแต่ละโดเมนของแกลเลียมอาร์เซไนด์

ลักษณะผิวหน้าของแกลเลียมอาร์เซไนด์ที่ปลูกบนแผ่นฐานเจอร์มาเนียมถูกศึกษาด้วยกล้องจุลทรรศน์ชนิด แรงอะตอม (Atomic force microscope) โดยพบว่าขนาดโดเมนของแกลเลียมอาร์เซไนด์จะแปรผันกับความ หนาของชั้นแกลเลียมอาร์เซไนด์ กล้องจุลทรรศน์อิเล็กตรอนแบบส่องผ่านได้ยืนยันว่ามีจุดบกพร่องหลายจุดที่บริเวณ รอยต่อระหว่างแกลเลียมอาร์เซไนด์และเจอร์มาเนียม คุณภาพของผลึกแกลเลียมอาร์เซไนด์ได้ถูกศึกษาโดยวิธีการหัก เหของรังสีเอ็กซ์เรย์ นอกจากนี้เราได้ทำการวัดคุณสมบัติทางกระแสไฟฟ้าเมื่อเทียบกับแรงดันไฟฟ้าที่ตกคร่อมชิ้นงาน โดยพบว่าชิ้นงานบางตัวอย่างแสดงคุณลักษณะแบบตัวต้านทานเชิงประกอบ ในขณะที่อีกบางตัวอย่างแสดงลักษณะ ของตัวตรวจจับแสง อีกทั้งเรายังได้ทำการวัดการตอบสนองต่อสเปกตรัมของแสงที่ตกกระทบบนชิ้นงานเพื่อศึกษา ช่วงความยาวคลื่นที่ชิ้นงานจะตอบสนองได้และสุดท้ายเราได้ทำการวัดคุณสมบัติในการเปล่งแสงของชิ้นงานพบว่า สเปกตรัมของแสงที่เปล่งออกมาจากชิ้นงานค่อนข้างซับซ้อน ทั้งนี้สืบเนื่องมาจากอิทธิพลของการแพร่ซึมของอะตอม ของแกลเลียม อาร์เซนิก และ เจอร์มาเนียม นอกจากนี้เรายังไม่สามารถตรวจพบการเปล่งแสงของควอนตัมดอตที่ปลูก บนแอนไทเฟสโดเมนของแกลเลียมอาร์เซไนด์ ซึ่งต้องทำการศึกษาในรายละเอียดที่ลึกลงไปในภายหน้า

ภาควิชา.........วิศวกรรมไฟฟ้า............ลายมือชื่อนิสิต...

สาขาวิชา.........วิศวกรรมไฟฟ้า............ลายมือชื่ออ.ที่ปรึกษาวิทยานิพนธ์หลัก......................

ปีการศึกษา...........2553...........
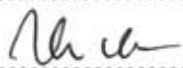
5070613621 : MAJOR ELECTRICAL ENGINEERING

KEYWORDS: GaAs / AlAs / Ge / MIGRATION-ENHANCED EPITAXY / MOLECULAR BEAM EPITAXY/ ANTI-PHASE DOMAINS

WICHIT TANTIWEERASOPHON : MOLECULAR BEAM EPITAXIAL GROWTH OF GaAs ON Ge SUBSTRATES FOR FUTURE PHOTONIC DEVICE APPLICATION. THESIS ADVISOR : PROF. SOMSAK PANYAKEOW, D.Eng., 78 pp.

GaAs is grown on Ge substrates by Molecular Beam Epitaxy (MBE) based on the fact that GaAs and Ge are lattice-matched materials. However, GaAs is a III-V compound semiconductor. When GaAs is grown on group IV Ge substrates, the anti-phase domain (APD) occurs due to randomness of group III and group V atoms grown as the first atomic layer at different seeding positions on Ge substrates. We investigate the growth conditions to obtain the large domains of GaAs epitaxial layer on Ge substrates. Migration-enhanced epitaxy (MEE) is used in our growth process. InAs QDs are grown on GaAs/Ge substrates having anti-phase domains (APDs). InAs QDs align in the specific crystallographic direction for each domain.

The morphology of GaAs on Ge substrates is observed by atomic force microscopy (AFM). Large domain size of GaAs can be obtained by varying the GaAs thickness. TEM images of GaAs on Ge samples are also investigated. The defects at the domain interfaces are observed. The crystal quailty of GaAs is studied by X-ray diffraction (XRD) method. Ohmic contacts and Schottky contacts to GaAs on Ge samples are prepared by the thermal evaporation. The I-V characteristics of the samples are measured showing resistive combined materials while another samples act as a photodetector. Photoconductivity measurements of GaAs on Ge samples are conducted to study their spectral responses. Photoluminescence (PL) of GaAs grown on Ge substrates is investigated. PL result does not show any emission peaks from InAs QDs.

Department ...Electrical Engineering.... Student's signature ....

Field of study ...Electrical Engineering... Advisor's signature ....

Academic year ....2010..................

Acknowledgements

CONTENTS

CONTENTS (continued)

LIST OF TABLES

LIST OF FIGURES

LIST OF FIGURES (continued)

LIST OF FIGURES (continued)

LIST OF FIGURES (continued)

LIST OF FIGURES (continued)

LIST OF FIGURES (continued)

ศูนย์วิทยทรัพยากร
จุฬาลงกรณ์มหาวิทยาลัย

LIST OF SYMBOLS

∇^2	Laplacian operator
AFM	atomic force microscope
AlAs	aluminium arsenide
AlGaAs	aluminium gallium arsenide
AlP	aluminium phosphide
APD	anti-phase domain
C	force constant of cantilever
δ	delta function
Δ	total spectrum broadening
Δz	cantilever deflection
$\Delta\gamma$	change of surface free energy
$D_{bulk}(E)$	bulk density of state
$D_{QW}(E)$	quantum well density of state
$D_{QWR}(E)$	quantum wire density of state
$D_{QD}(E)$	quantum dot density of state
D.O.S.	density of states
ε	misfit
E	carrier energy
E_{kin}	kinetic energy
E_0	characteristic energy
E_n	quantized energy
$E_{n,x}$	quantized energy in x-direction
$E_{n,y}$	quantized energy in y-direction
$E_{n,z}$	quantized energy in z-direction
F	force exerted on the tip
F_{ω}	applied driving force amplitude
FWHM	full width at half maximum
fcc	face-centered-cubic

LIST OF SYMBOLS (continued)

$\boldsymbol{G}$	reciprocal lattice vector
GaAs	gallium arsenide
GaP	gallium phosphide
Ge	germanium
g^{sat}	maximum optical gain
HRXRD	High resolution X-ray diffraction
h	Plank's constant
$\bar{h}$	reduced Plank's constant
h_c	critical thickness
InAs	indium arsenide
InGaAs	indium gallium arsenide
InP	indium phosphide
InGaP	indium gallium phosphide
k, k_B	Boltzmann's constant
λ	de Broglie wavelength
	or elastic modulus
$\mathbf{k} = (k_x, k_y, k_z)$	wave vector
k	amplitude of wave vector
$\boldsymbol{k}_{in}$	wave vectors of the incident electrons
$\boldsymbol{k}_{diff}$	wave vector of diffracted electrons
$k_{//}$	amplitude of in-plane (y-z) wave vector
L	macroscopic length scale
L_x	nanometer length scale in x direction
L_y	nanometer length scale in y direction
L_z	nanometer length scale in z direction
L_{QW}	sum of the well and barrier regime thickness
LED	light emitting diode
M	molecular weight

LIST OF SYMBOLS (continued)

MBE	molecular beam epitaxy
MEE	migration-enhanced epitaxy
MOCVD	metal organic chemical vapor deposition
m^*	effective mass
m_{eff}	carrier effective mass
N_{wi}	area density of the quantum wires
N_D	volume density of quantum dots
N_e	number of states per unit surface
n	quantum number
$\emptyset$	impingement rate
PBN	pyrolytic boron nitride
PL	photoluminescence
p	carrier momentum
Q	quality factor of the oscillator
QE	quantum efficiency
QD	quantum dot
QW	quantum well
QWR	quantum wire
$\mathbf{r} = (x,y,z)$	carrier position vector
SEM	scanning electron microscopy
SiGe	silicon germanium
SK	Stranski-Krastanov
Θ	Heaviside's unit step function or amounts of surface coverage
θ	Bragg diffraction angle
T	temperature
t_b	monolayer deposition times of the beams
t_{res}	background residual vapor
UHV	ultra high vacuum

LIST OF SYMBOLS (continued)

$V(\mathbf{r})$ confinement potential

ω_o resonance frequency

$\varphi(\mathbf{r})$ envelope wave function

$\varphi_n(x)$ wave function for the particular energy level n

WL wetting layer

XRD X-ray diffraction

ZnSe zinc selenide

z_ω magnitude of the cantilever response at a frequency ω

CHAPTER I

INTRODUCTION

Lattice mismatch between GaAs and Ge is 0.1 % leading to the possibility of forming defect-free heterostructure. Nevertheless, GaAs is a polar, III-V compound semiconductor whereas Ge is a non-polar, IV elemental semiconductor. The polar/non-polar heterointerface leads to anti-phase domains (APDs) in GaAs epitaxial layer grown on Ge substrates. The APDs can be eliminated by using miscut Ge substrate [1].

In this work, we report the effect of APDs and the crystalline quality of GaAs/Ge heterojunction grown by migration-enhanced molecular beam epitaxy (MEE) [2] where group III and group V elements are alternately supplied at different duration times. With the suitable growth conditions, we could obtain the large GaAs crystal domains on Ge substrates. A combination of GaAs and Ge materials is applicable for many optoelectronic devices due to their bandgap properties, i.e. direct/indirect, wide/narrow bandgaps and their electronic properties, i.e. electron mobility, carrier life times, etc.

GaAs on Ge is a good candidate for tandem solar cells [3-5] in which GaAs part absorbs short wavelengths and Ge works for the remaining long wavelengths as the bottom cell. Tandem solar cells, therefore, have wide spectral response with good cell performance. Many III-V compound semiconductors on Ge solar cells are widely used in space applications [6] and concentrated terrestrial systems [7].

Self-assembled InAs quantum dots (QDs) grown on GaAs substrate are used as the active region of lasers [8-10] amplifiers [11,12], infrared detectors [13,14], and in other device applications [15,16]. Recently, Dhawan et al [17] reported the growth of InAs quantum dots on germanium substrate by metal organic chemical vapor deposition (MOCVD) and Knuuttila et al [18] reported the growth of non-uniformly distributed InAs islands directly on Ge substrate without any buffer layer. In the growth of InAs QDs directly on Ge substrate, the formation of anti-phase domains is avoided since the dot formation occurs after a thin wetting layer is grown. Many defects will be in this thin wetting layer. This may adversely influence the growth of good quality dots later.

Buffer layer assists in decreasing the surface defects of the substrate and help in confining InAs QDs. However, the growth of uniformly distributed InAs QDs on standard (001) Ge substrates using GaAs buffer layer is rarely reported. InAs QDs are typically grown on miscut Ge substrates using GaAs buffer layer because APDs can be reduced or even eliminated using miscut Ge substrates. Motivated by the fact that on-axis Ge (001) substrates are cheaper and more widely used, we report the growth of InAs QDs on on-axis Ge (001) substrates using GaAs buffer layer and AlAs interfacial layer which proves to be effective as a blocking layer, preventing the cross diffusion of Ge, Ga and As atoms [19].

CHAPTER II

THEORY

Due to the continued development in nanotechnology, the novel semiconductor structures are fabricated with subnanometer accuracy and precisely controlled the electronic and optical properties. This progress in nanoscale engineering, as well as an improved understanding of the physical phenomena at the nanometer scale, has contributed to the rapid development of low-dimensional physics of semiconductor.

In this chapter, the basics concept of quantum dot (QD) structure and anti-phase domain (APD) are reviewed. Quantum dots are nanostructure which contains a tiny droplet of free electrons. Their typical dimensions are between nanometers to a few microns. Just as in an atom, the energy levels are quantized due to the confinement of electrons. The 3D spatial confinement is observed in the quantum dots.

Anti-phase domain is the region where the atomic arrangements are of the opposite to that of perfect lattice system. Polar/non-polar hetero interface leads to anti-phase domains in epitaxial layer. Finally, p-n junction properties are briefly discussed.

2.1 Low-Dimensional Nanostructures

When the carrier motions in a solid is limited in a layer of a thickness of the order of the carrier de Broglie wavelength, effect of size quantization emerges. The de Broglie wavelength λ depends on the effective mass m_{eff} of the carrier and on temperature T:

$$\lambda = \frac{h}{p} = \frac{h}{\sqrt{3m_{eff}kT}} = \frac{1.22 \text{ nm}}{\sqrt{(E_{kin}/[eV])}} \qquad (2.1)$$

Where h is Planck's constant, p is carrier momentum, and k_B is Boltzmann's constant. The mass of charged carriers in Eq. (2.1) is not the free electron mass but the effective mass of the electron (or hole) in the crystal. As this mass can be much smaller than the free electron mass, size quantization effects can be already pronounced at a thickness ten

to a hundred times larger than the lattice constant. The de Broglie wavelength for electrons in III-V semiconductor materials is in the order of 20 nm at 300 K.

When the size or dimension of a material is continuously from a macroscopic size, such as a meter or a centimeter, to a very small size, the properties remain the same at first, then small changes begin to occur, until finally when the size drops below 100 nm, dramatic changes in properties can occur. If one dimension is reduced to the nanometer range while the other two dimensions remain large, then a structure known as a quantum well is obtained. If two dimensions are so reduced and one remains large, the resulting structure is referred to as a quantum wire. The extreme case of this process of size reduction in which all three dimensions reach the low nanometer range is called a quantum dot. The word *quantum* is associated with these three types of nanostructures because the changes in properties arise from the quantum-mechanical nature of physics in the domain of the ultra-small. Fig. 2.1 shows a schematic comparison between a bulk semiconductor, a waveguide for visible light, a QD, and an atom.
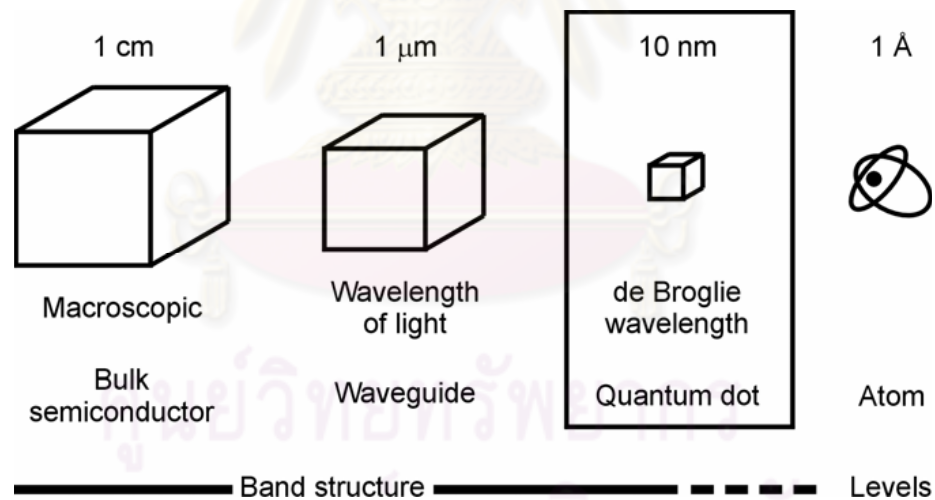
Fig 2.1 A schematic comparison between a bulk semiconductor, a waveguide for visible light, a QD, and an atom [20].

In the case of atom, the electronic structure is described by discrete energy levels, while band theory is used in the case of bulk semiconductor. Since the structural size is varied continuously, there exists an explanation between two cases (discrete levels and

continuum band structure). The density of state of bulk semiconductor and low-dimensional nanostructure is shown in Fig. 2.2. The band offsets between the low-dimensional nanostructures and the surrounding material provide the energy potential or potential well in energy band to confine the carriers. Thus the carrier motion is limited in this direction and allowed to move freely only in bulk dimension, which exists no potential well. Electrons and holes in a quantum well can freely move in the *x-y* plane; those in a quantum wire can only move in *x* direction. In a QD, zero-dimensional-nanostructure, the charge carriers are completely localized. This 3-D confinement results in a quantization of the carrier energy and in a variation of the carrier density of states.
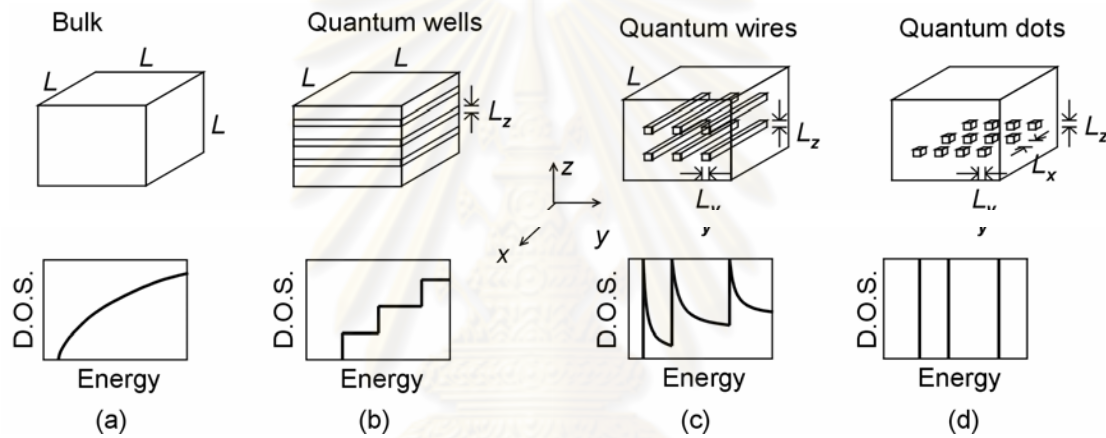
Fig 2.2 Schematic diagram illustrating the representation of the electronic density of states depending on dimensionality. (a) bulk, (b) quantum wells, (c) quantum wires, and (d) QD and their density of states (D.O.S.) [21]. L is in macroscopic scale (~cm), while L_x, L_y, L_z, are in nanoscale.

The quantization phenomenon can be described by wave-like properties of electrons, since any substance would exhibit its wave properties of which de Broglie wave length can be calculated from eq. (2.1). Electrons are delocalized in a bulk semiconductor. These electrons are referred to as *free electrons*, but perhaps unconfined electrons would be a better word for them. This is because when the size of semiconductor diminishes to the nanoscale, these electrons begin to experience the effects of confinement, meaning that their motion becomes limited by the physical size of

the region or domain in which they move. The influence of electrostatic forces becomes more pronounced, and the electrons become restricted by a potential barrier that must be overcome before they can move more freely. More explicitly, the electrons become sequestered in what is called a *potential well*, an enclosed region of negative energies. A simple model that exhibits the principal characteristics of such a potential well is a square well in which the boundary is very sharp or abrupt. Square wells can exist in one, two, three, or higher dimensions.

Standard quantum-mechanical calculations show that for an infinitely deep square potential well of width L_z in one dimension, the coordinate x has the range of values $-\frac{1}{2}L_z \leq x \leq \frac{1}{2}L_z$ inside the well, and the energies there are given by the expressions

$$E_n = \left[\frac{\pi^2 \bar{h}^2}{2mL_z^2}\right] n^2 \tag{2.2}$$

$$= E_o n^2 \tag{2.3}$$

which are plotted in Fig 2.3, where $E_o = \pi^2 \bar{h}^2 / 2mL_z^2$ is the ground-state energy and the quantum number *n* assumes the values *n* = 1, 2, 3, …. The electrons that are presented and fill up the energy levels starting from the bottom, until all available electrons are in place. An infinite square well has an infinite number of energy levels, with ever-widening spacing as the quantum number *n* increases. If the well is finite, then its quantized energies E_n all lie below the corresponding infinite well energies, and there are only a limited number of them.

The electrons confined to the potential well move back and forth along the direction *x*, and the probability of finding an electron at a particular value of *x* is given by the square of the wavefunction $|\varphi_n(x)|^2$ for the particular level *n* where the electron is located. There are even and odd wavefunctions $\varphi_n(x)$ that alternate for the levels in the one-dimensional square well, and for the infinite square well the unnormalized expressions are given by

$$\varphi_n = \cos(n\pi x/L_z) \qquad n = 1, 3, 5, \ldots \text{ even parity} \tag{2.4}$$

$$\varphi_n = \sin(n\pi x/L_z) \qquad n = 2, 4, 6, \ldots \text{ odd parity} \tag{2.5}$$
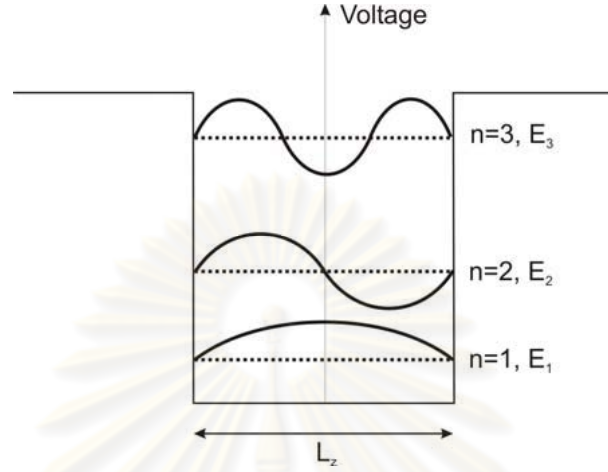
Fig 2.3 Schematic representation of the lowest three level of carrier's energy quantization in potential well with the width of L_z (comparable to de Broglie wavelength). The picture shows examples of the three lowest-energy standing waves which can be happened in potential well (solid line) and the corresponding carrier's energy level of the de Broglie wavelength from the standing wave (dotted line), i.e. E_1, E_2 and E_3. The energy of each level is given by $E_{n,z} = n^2 \pi^2 \bar{h}^2 / 2mL_z^2$, where n is an integer number of the level.

An effective-mass approximation can effectively describe the electronic states of bulk semiconductors. In semiconductor quantum wells, this approximation is widely used for the calculation of quantized energy levels [22]. The main assumption of the effective-mass approximation is that the envelope wave function does not significantly vary in the unit cell with a length scale of subnanometers. Therefore, this assumption is valid in all low-dimensional nanostructures. Assuming parabolic band dispersion, band-edge electron states of semiconductors can be described by Schrödinger-like equation as

$$\left[\frac{\bar{h}^2}{2m^*} \nabla^2 + V(\mathbf{r}) \right] \varphi(\mathbf{r}) = E\varphi(\mathbf{r}) \tag{2.6}$$

where m^* is the effective mass, $\bar{h}$ is reduced Planck's constant, $\mathbf{r} = (x,y,z)$ is the carrier position vector, $V(\mathbf{r})$ is the confinement potential due to band offset, $\varphi(\mathbf{r})$ is the envelope wave function, and E is carrier energy.

From eq. (2.6), by assuming the barrier potentials with *infinite height*, the carrier energy E and density of states per unit volume (D.O.S.) (the number of states between the energy E and $E + dE$, of each quantum nanostructure) in case of bulk, quantum well (QW), quantum wire (QWR) and QD can be written as follow [21],

Bulk semiconductors

$$E_{bulk} = E(\mathbf{k}) = \frac{\bar{h}^2 k^2}{2m^*} \tag{2.7}$$

$$D_{bulk}(E) = \frac{1}{2\pi^2}\left[\frac{2m^*}{\bar{h}^2}\right]^{\frac{3}{2}} E^{\frac{1}{2}} \tag{2.8}$$

where $\mathbf{k} = (k_x,k_y,k_z)$ is the wave vector of carriers and $k^2 = k_x^2 + k_y^2 + k_z^2$

Quantum Well (QW)

Assuming that the confinement potential barrier for the square QW has infinite height, we obtain

$$E_{QW} = E(\mathbf{k}) = \frac{\bar{h}^2 k_{//}^2}{2m^*} + E_{n,z} = \frac{\bar{h}^2}{2m^*}\left(k_{//}^2 + \left(\frac{n_z\pi}{L_z}\right)^2\right) \tag{2.9}$$

$$D_{QW}(E) = \frac{m^*}{\pi\bar{h}^2 L_{QW}} \sum_{n_z} \Theta\left(E - E_{n_z}\right) \tag{2.10}$$

where $k_{//}^2 = k_x^2 + k_y^2$, Θ is the Heaviside's unit step function, $n_z = 1, 2, 3,\ldots$ and L_{QW} is the sum of the well and barrier regime thickness.

Quantum Wires

Assuming that the confinement potential barrier for the square quantum wires has infinite height, we get

$$E_{QWR} = E(\mathbf{k}) = \frac{\bar{h}^2 k_\perp^2}{2m^*} + E_{n_y} + E_{n_z} = \frac{\bar{h}^2}{2m^*}\left(k_\perp^2 + \left(\frac{n_y\pi}{L_y}\right)^2 + \left(\frac{n_z\pi}{L_z}\right)^2\right) \qquad (2.11)$$

$$D_{QWR}(E) = \frac{N_{wi}\sqrt{2m^*}}{\pi\bar{h}} \sum_{n_y,n_z} \frac{1}{\sqrt{E - E_{n_y} - E_{n_z}}} \qquad (2.12)$$

where $k_\perp^2 = k_x^2$, n_y, $n_z = 1, 2, 3,\dots$ and N_{wi} is the area density of the quantum wires (the number of quantum wires divided by the quantum-wire region area in the *y-z* plane).

Quantum Dot

Assuming that the infinite confinement potential barrier in all direction, we obtain

$$E_{QD} = E_{n_x} + E_{n_y} + E_{n_z} = \frac{\bar{h}^2}{2m^*}\left(\left(\frac{n_x\pi}{L_x}\right)^2 + \left(\frac{n_y\pi}{L_y}\right)^2 + \left(\frac{n_z\pi}{L_z}\right)^2\right) \qquad (2.13)$$

$$D_{QD}(E) = 2N_D \sum_{n_x,n_y,n_z} \delta\left(E - E_{n_x} - E_{n_y} - E_{n_z}\right) \qquad (2.14)$$

where δ is the delta function, and N_D is the volume density of QDs.

The change of density of states for the low-dimensional nanostructures considerably affects the fundamental properties of the devices, which use these nanostructures as an active layer [23]. The electronic properties for QD structure is dramatically different from the bulk semiconductors because of the discrete energy levels and delta peak density of states, which are in contrast to the continuous spectrum of the

bulk. In case of QD structures, there are several theoretical and experimental proves that semiconductor lasers consisting of QD structures have the lowest threshold current density due to the delta-function-like density of states [24].

To utilize QDs as an active layer for semiconductor lasers, two particularly important considerations must be included. Firstly, the density of QDs must be sufficiently high to achieve the lasing condition (gain overcomes the loss). Secondly, the QD size distribution should be narrow since the optical gain spectra depend on the size distribution. In other words, QDs should have the same size in order to decrease the charge carriers needed for the population inversion condition. The maximum optical gain, g^{sat}, for a QD laser can be written as [25]

$$g^{sat} \propto \frac{N_e}{\Delta} \tag{2.15}$$

where N_e is the number of states per unit surface. For the ground level, N_e is equal to the doubled surface density of the QD array, N_D. Δ is the total spectrum broadening from all excited QDs. From eq. (2.15), it is possible to increase the maximum optical gain by increasing the QD density and/or reducing the size distribution of the QD ensemble.

In summary, we introduced the concept of low-dimensional nanostructures, i.e. QWs, QWRs, and QDs compared with bulk semiconductors. The general theoretical view of the size and the electronic properties, i.e., density of states was presented.

2.2 Self-Assembled Growth

The self-assembled growth is the QD fabrication technique which is used in this thesis work. The growth mode and growth conditions for this growth technique are reviewed in order to provide some basic understanding of this growth method.

2.2.1 Growth Modes

From the typical theory of crystal growth by molecular beam epitaxy, three modes of crystal growth on the surface are possible [26]. If we denote the free energy of the epilayer/vacuum interface by γ_e, that of the epilayer/substrate interface by γ_i, and that of the substrate/vacuum interface by γ_s, the layer-by-layer growth mode is favoured if

$$\Delta\gamma = \gamma_e + \gamma_i - \gamma_s < 0 \qquad (2.16)$$

In this case, as epilayers are nucleated, the free energy decreases initially before achieving a steady-state value for thicker films. Alternatively, if $\Delta\gamma > 0$ the deposited material would prefer to cover the substrate surface, then we obtain Frank Van der Merwe growth mode or layer-by-layer growth (Fig 2.4(b)). In this mode, the interaction between the substrate and deposited atoms is stronger than that between neighboring atoms. In contrast, if $0 < \Delta\gamma$, the 3D growth mode as Volmer Weber mode is observed (Fig 2.4(a)), where the interaction between substrate neighboring atoms exceeds the overlayer substrate interactions.
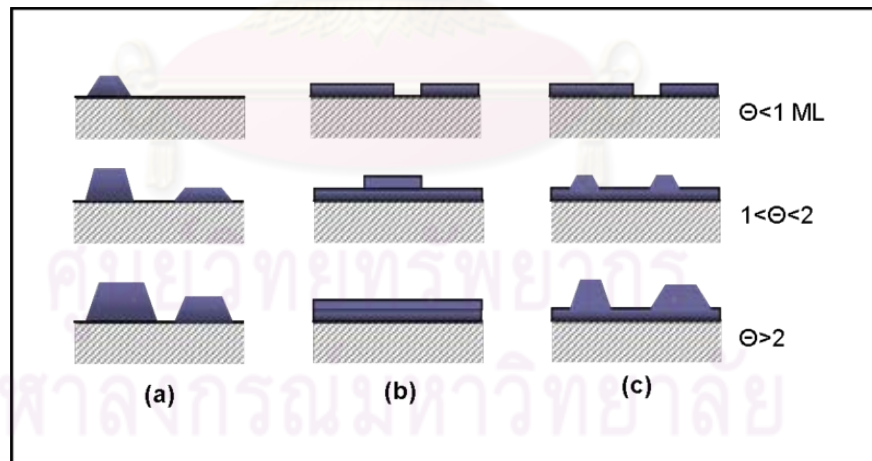
Fig 2.4 Cross-section views of the three primary modes of thin film growth including (a) Volmer-Weber (VW: island formation), (b) Frank-van der Merwe (FM: layer-by-layer), and (c) Stranski-Krastanov (SK: layer-plus-island). Each mode is shown for several different amounts of surface coverage, Θ.

In case of layer-plus-island or Stranski-Krastanov growth mode (Fig 2.4(c)), the growth exhibits an intermediate case. After forming a few monolayers in layer-by-layer growth mode, the islands are nucleated on top of this "intermediate" layer, which is called the wetting layer (WL). The explanation on this growth mode is reviewed in the next section.

2.2.2 Self-Assembled Growth in Stranski-Krastanov Mode

Stranski-Krastanov is one of the three primary modes by which thin films are grown epitaxially at a crystal surface or interface. Also known as layer-plus-island growth, the SK mode follows a two step process. Initially, complete films of adsorbates, up to several monolayers thick, are grown in a layer-by-layer fashion on a crystal substrate. Beyond a critical layer thickness, which depends on strain and the chemical potential of the deposited film, growth continues through the nucleation and coalescence of adsorbate islands.

In this section, we investigate the detail of Stranski-Krastanov growth mode, which provides defect-free self-assembled QD structures. The illustration of the film growth in this mode is shown in Fig 2.5. First, a few monolayers of strained material grow in layer-by-layer mode. During the growth, elastic strain energy, E(el) builds up due to the lattice mismatch, which is given by [27].

$$E(el) = \lambda\varepsilon^2 At \qquad\qquad (2.17)$$

where λ is the elastic modulus, ε is the misfit, and A is surface area. The total energy for the layer-by-layer growth increases as a function of the film thickness t. Beyond the critical thickness, the layer-by-layer growth is unfavorable, and so elastic strain relaxation occurs. The local strain energy density of the SK-growth mode QD is schematically represented in Fig 2.6. The nanoscale islands formed in this mode can be used to confine carrier in three dimensions. The nanostructures formed in the Stranski-Krastanov mode are called self-assembled QDs.

13
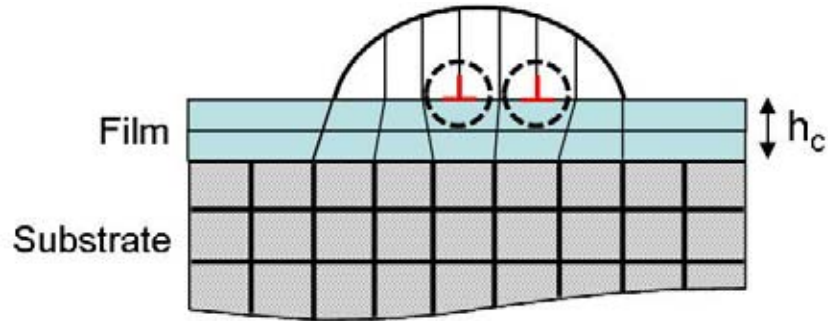
Fig 2.5 SK growth showing island formation after obtaining a critical thickness, h_c. Lines represent lattice planes with thicker lines for the substrate lattice and thinner lines for the growing film. Edge dislocations are indicated inside the dash circle.
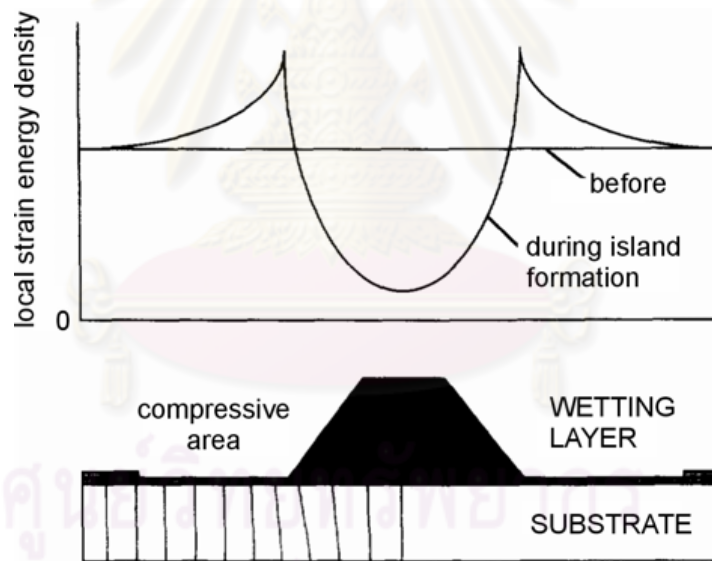
Fig 2.6 Schematic representation of the local strain energy density in and around the SK-growth mode QD. The energy barrier has a maximum at the edge of the QD.

Although the QDs grown by this technique form into high-density arrays. There are still some disadvantages of this technique. For example, the Stranski-Krastonov growth mode QDs exhibit wide size distribution which respond to varying of energy level

in the energy band. The representations of the energy level exhibited in the QD with different size are shown in Fig 2.7. Also, the non-uniform strain distribution from lattice-mismatched formation would effect on the band structure of QD [28]. Both are undesirable for laser applications.
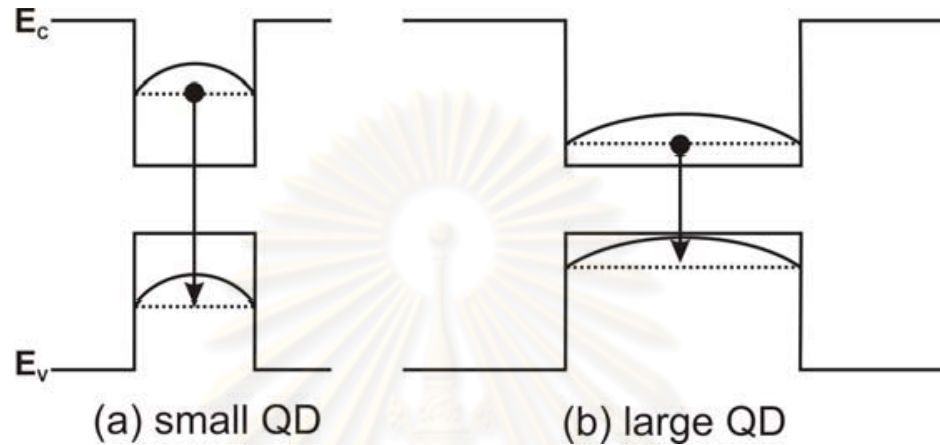
Fig 2.7 Simple interpretation of the energy level exhibited in the QD with different size. The representations in case of (a) small QD show the higher energy level than that of large QD (b) due to the carrier confinement properties. Electrons and holes in a small size QD would exhibit shorter de Broglie wavelength of which corresponding energy level is higher.

2.2.3 Migration-Enhanced Epitaxy (MEE)

Migration of surface adatoms along the surface is very important for growing high quality layers and atomically flat heterojunctions. In the migration-enhanced epitaxy (MEE) of GaAs or AlGaAs, migration of Ga and Al atoms is enhanced even at low substrate temperatures by evaporating them onto a clean GaAs surface under an As-free or low As pressure atmosphere. Fig 2.8 shows schematic display of the migration process of Ga atoms deposited on the vicinal surface. Thus, the high quality GaAs and AlGaAs layers and flat heterojuntions have been grown by this method. Migration-enhanced epitaxy has also proved useful in investigating atomic processes during the epitaxial growth. Horikoshi et al. have proposed this growth method, which is characterized by

alternately supplying Ga and/or Al and As to the substrate [29-31]. They have shown that it greatly increase the Ga or Al surface diffusion by reducing the As supply, and thus it is useful for growing high quality GaAs or AlGaAs layers even at low substrate temperatures. So far, The MEE process has been investigated mainly by reflection high-energy electron diffraction (RHEED) [29-31]. Yoshikazu et al. have analyzed the MEE growth mechanism in real-space observation using in situ scanning electron microscopy (SEM) [32].
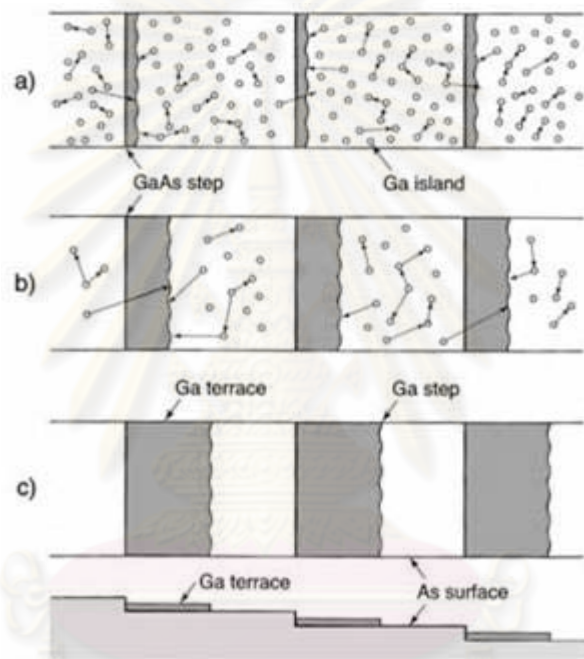
Fig 2.8 Schematic display of the migration process of Ga atoms deposited on the vicinal surface. (a) Immediately after Ga deposition is terminated, (b) during annealing, (c) after long time annealing (Horikoshi, JCG 1999.).

The epitaxial growth is a process in which atoms randomly deposited on the growing surface are properly arranged according to the equilibrium atomic configuration on the substrate surface. Any departure from the perfect arrangement induces crystal imperfections. Therefore, the lateral migration of deposited atoms along the surface is very important for growing high quality layers. In molecular beam epitaxy (MBE), the growth of GaAs is performed by the simultaneous deposition of the constituent atoms and

molecules under As-stable conditions. Under these conditions, the growing surface is covered with a large number of GaAs islands, because Ga atoms deposited on the growing surface react with As to form small GaAs islands. These small islands hardly move along the surface because of the stable chemical bonds between GaAs molecules in the islands and As atoms in the underlying As plane. Even in this case, however, there is an equilibrium density of isolated Ga atoms on the growing surface [33]. These isolated Ga atoms are nucleated in such a way that As molecules are re-evaporated at the periphery of the small islands because of the increased surface energy caused by the island formation. This process involves isolated Ga atoms. In addition, deposited Ga atoms have a finite lifetime before they react with As. These isolated Ga atoms are quite mobile and easily migrate to the more stable sites. This process is essential to the growth of high quality layers, but requires a substrate temperature high enough to guarantee re-evaporation of As molecules at the periphery of the islands. However, the deposition of Ga atoms in an As-free atmosphere supplies a large number of mobile Ga atoms on the growing surface. These Ga atoms are expected to migrate along the surface even at reduced temperatures, and to find stable sites on the surface [29]. Therefore, high quality layers can be grown after the succeeding As_4 deposition even at very low substrate temperatures. Migration-enhanced epitaxy (MEE) is based on this principle [30]. Schematic of MEE process is shown in Fig 2.9. In addition, the low temperature growth by MEE opened a way to construct new types of superlattice heterostructures between different materials such as GaAs/ZnSe superlattices [34] and $(GaAs)_{l-x}(Si_2)_x$/GaAs superlattices [35].
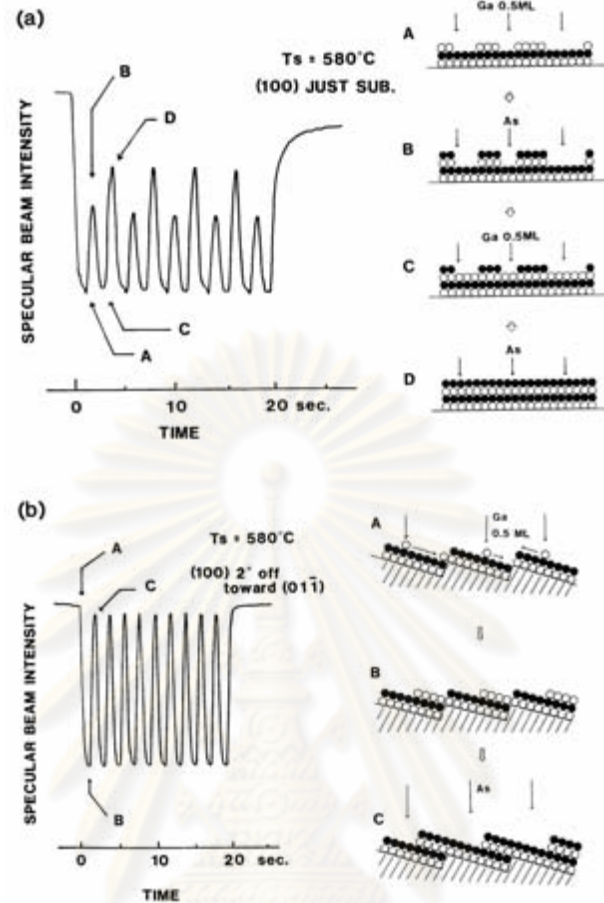
Fig 2.9 Schematic of MEE process with RHEED specular beam oscillation on
(a) oriented and (b) misoriented GaAs substrate (Yamaguchi et al.,
JJAP 1989).

At temperatures higher than 550°C, isolated Ga atoms have long enough lifetimes
for flat surfaces to be grown even by conventional MBE if the growth conditions are
carefully optimized. The effect of MEE would therefore be less pronounced at high
growth temperatures.

2.2.4 Material Considerations

Self-assembled growth can be carried out in several semiconductor material
systems, e.g., In(Ga)As/GaAs, InP/InGaP, or SiGe/Si. The preliminary condition for the

growth is that the QD material has a larger lattice constant and a smaller band gap compared with the substrate material. Fig 2.10 shows the band energy as a function of lattice constant for the III-As material systems. For laser applications in optical communication systems, GaAs is the most important substrate material. The self-assembled growth of InAs on GaAs substrate can provide QDs, which emit light at 1.3 µm or longer wavelength. In this work, we will concentrate only on the InAs/GaAs material system.
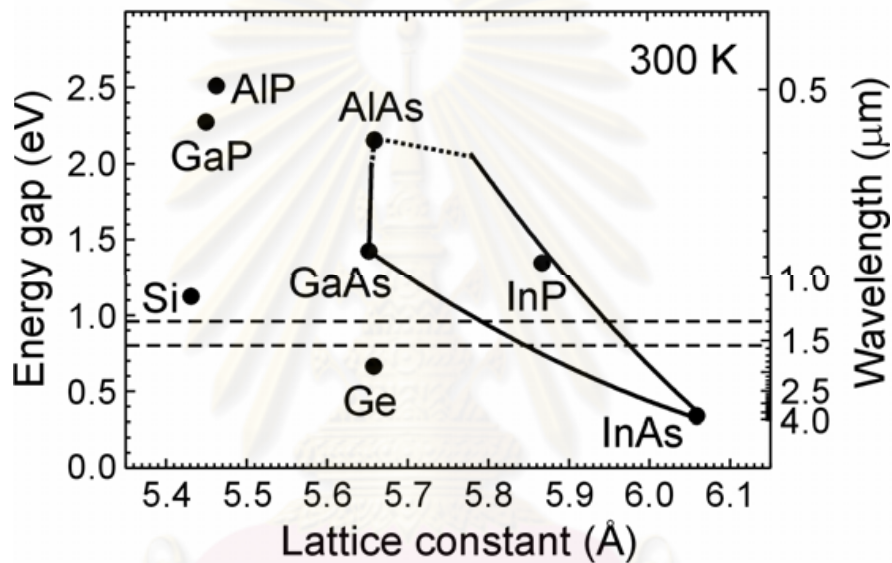
Fig 2.10 Lattice constant versus energy gap at room temperature for the III-As material system. The solid line is for direct band gap material and the dotted line is for indirect band gap material. From this figure we can see that there is a possibility to realize QD structures which emit light at the wavelength of 1.3 µm or 1.55 µm (dashed lines).

2.3 Anti-Phase Domains (APDs)

Lattice mismatch between GaAs and Ge is 0.1 % leading to the possibility of forming defect-free heterostructure. However, GaAs is a polar, III-V compound semiconductor whereas Ge is a non-polar, IV elemental semiconductor. The polar/non-

polar heterointerface leads to anti-phase domains (APDs) in GaAs epitaxial layer grown on Ge substrates. The APDs can be eliminated using miscut Ge substrates [1].
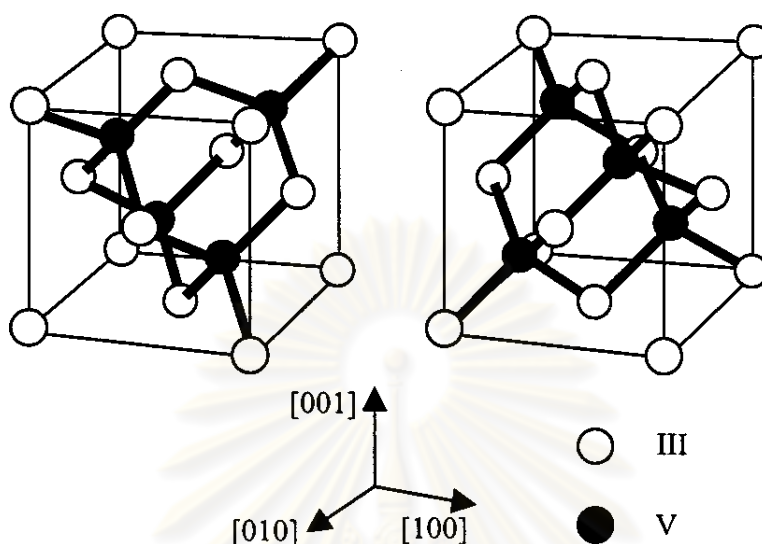
Fig 2.11. Two possible orientations of the zinc-blende crystal structure common to many of the III–V compound semiconductors, including GaAs. Each distinct orientation corresponds to a 90° rotation of the lattice, or a switching of the cation and anion sublattices.

Although the lattice mismatch does not play an important role in affecting the quality of GaAs/Ge epitaxy, compound semiconductor growth on elemental substrate poses several unique challenges, including the effect of antiphase disorder [36]. Due to the inequivalence of its two face-centered-cubic (fcc) sublattices, the zince-blende crystal structure of GaAs and other III-V compounds possesses lower symmetry than the diamond cubic structure. Therefore, when GaAs is grown on a Ge substrate, two sublattice orientations occur, see Fig. 2.11, each rotated 90° with respect to the other, corresponding to a switching of the cation and anion sublattices.

When both GaAs orientations are nucleated on a Ge substrate, distinct domains of each sublattice, separated by antiphase boundaries (APBs) may penetrate well into the GaAs epilayer as illustrated in Fig 2.12. Since APBs are comprised of planes of wrong nearest-neighbor bonds, they are electrically active defects known to cause carrier scattering and non-radiative recombination [37-38]. As a result, any effort to grow device

quality GaAs/Ge must address the possibility of anti-phase disorder and the methods to eliminate it.
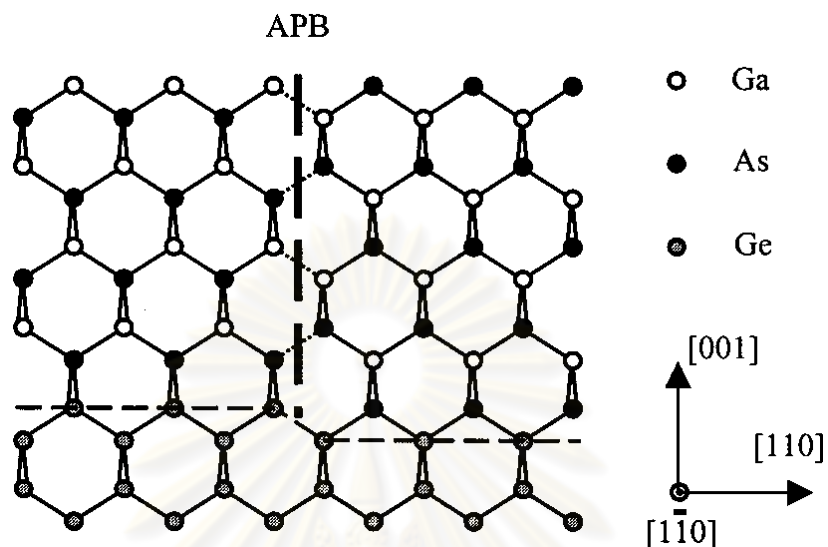
Fig 2.12 A GaAs APB nucleated by the sublattice displacement induced by a single atomic-layer step lying on the (001) Ge surface. The bold dashed line marks the wrong nearest-neighbor bonds lying on the plane of the APB.

The effective mean to suppress antiphase disorder requires control of the substrate surface structure prior to GaAs growth. The surface of (001) Ge, like that of Si, is structurally characterized by dimer reconstructed terraces separated by steps [39-40]. Pairing or dimerization, of adjacent fourfold coordinated Ge atoms exposed on the (001) surface reduces the number of dangling bonds per atom from two to one and is therefore energetically favorable. The presence and distribution of steps running along the in-plane <110> directions indicates any deviation of the surface from the exact (001) orientation. A two-domain (001) surface, illustrated in Fig. 2.13(a), features single or any odd-integer number of atomic-layer steps, such that on alternating terraces, the exposed sublattice domain shifts, rotating the dimer bonds by 90°.
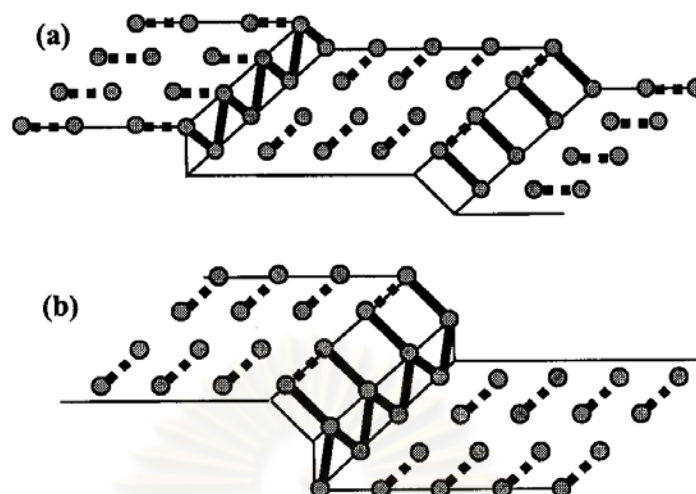
Fig 2.13 Double-domain (a) and single-domain (b) reconstructed surfaces of (001) Ge.
Note that the orientation of dimer bonds (dashed lines) rotates 90° as the
sublattice switches on alternating terraces of the two-domain surface, whereas
only one dimer orientation and one sublattice is evident on the single-domain
surface.

(001) Ge and Si substrates intentionally offcut to [110] are widely believed to promote
single-domain GaAs growth. In contrast to the actual (001) surface, which features
irregular steps along the <110> directions, a substrate offcut towards [110] introduces a
regular array of surface terraces separated by single-steps running along the [1-10]
direction. As the offcut angle is increased, the density of steps and width of surface
terraces decreases, a factor that may by itself promote early self-annihilation of APBs.
However, it has also been known for some time that at high temperatures under ultrahigh
vacuum (UHV) conditions, offcut Ge and Si (001) surfaces favor a single-domain
reconstruction which may extend to single-domain GaAs nucleation.[39-41] As shown in
Fig 2.13(b), this configuration consists of double atomic layer steps separating terraces of
the same exposed sublattice where all dimers lie parallel to the step edges. Although there
exist discrepancies in the literature regarding the exact mechanism of anti-phase disorder
suppression, in general, substrate offcut is expected to enhance surface transition kinetics,
thereby diminishing the possibility of APB nucleation and propagation.

Arsenic and arsenic precursors used in GaAs growth are known to interact with Ge and Si surfaces and thus present an additional complication to the anti-phase problem [42-45]. On reconstructed (001) Ge and Si surfaces, arsenic atoms readily adsorb and dimerize in the place of substrate atoms. Each atom of an arsenic dimer features a lone pair of electrons rather than a dangling bond, resulting in a net surface energy decrease. The resulting arsenic passivated surface is highly inert and self-limited to a single monolayer of coverage. However, it has been noted in numerous studies that arsenic coverage results in considerable modification of the pre-existing substrate step structure, with strong implications for single-domain GaAs growth.

2.4 p-n Junction

This section briefly discusses about p-n junction properties. A p–n junction is formed by joining p-type and n-type semiconductors together in very close contact. The term *junction* refers to the boundary interface where the two regions of the semiconductor meet. If they were constructed of two separate pieces this would introduce a grain boundary, so p–n junctions are created in a single crystal of semiconductor by doping, for example by ion implantation, diffusion of dopants, or by epitaxy (growing a layer of crystal doped with one type of dopant on top of a layer of crystal doped with another type of dopant).

p-n junctions are elementary "building blocks" of almost all semiconductor electronic devices such as diodes, transistors, solar cells, LEDs, and integrated circuits. They are the active sites where the electronic action of the device takes place. For example, a common type of transistor, the bipolar junction transistor, consists of two p–n junctions in series, in the form n–p–n or p–n–p.

The p–n junction possesses some interesting properties which have useful applications in modern electronics. A p-doped semiconductor is relatively conductive. The same is true of an n-doped semiconductor, but the junction between them can become depleted of charge carriers, and hence non-conductive, depending on the relative voltages of the two semiconductor regions. By manipulating this non-conductive layer, p–n junctions are commonly used as diodes: circuit elements that allow a flow of

electricity in one direction but not in the other (opposite) direction. This property is explained in terms of forward bias and reverse bias, where the term bias refers to an application of electric voltage to the p–n junction. Properties of the p-n junction are shown in Fig 2.14.
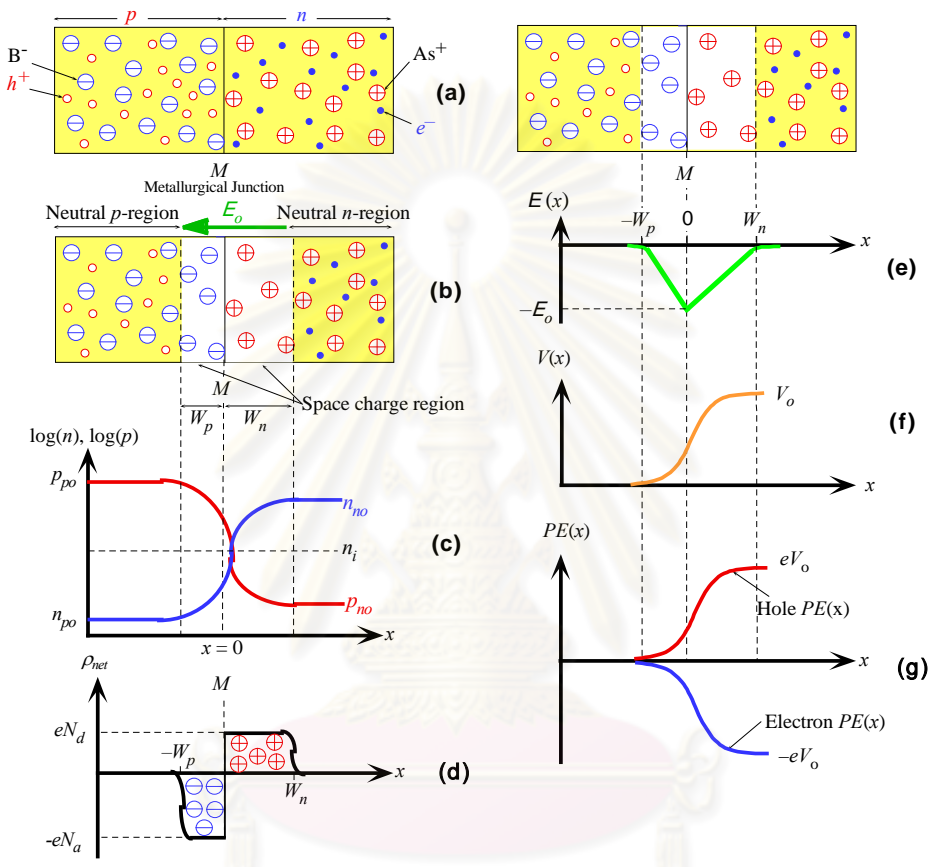
Fig 2.14 Properties of the p-n junction. (© 1999 S.O. Kasap, *Optoelectronics* (Prentice Hall)).

CHAPTER III

EXPERIMENTAL DETAILS

3.1 Basics of Molecular Beam Epitaxy (MBE)

Molecular be am epi taxy is a pr ocess f or e pitaxial g rowth via the int eraction of one or several molecular or atomic beams that occurs on a surface of a heated crystalline substrate unde r ul tra-high vacuum c onditions ($\sim 10^{-8}$ Pa). MBE can achieve precise control of chemical c ompositions a nd dopi ng p rofiles. S ingle-crystal, multilayer structures with dimension on the order of atomic layer can be grown by MBE. Thus, the MBE enables the precise fabrication of semiconductor heterostructures having thin layers from a fraction of a micron down to a monolayer. Fig 3.1 shows a schematic of typical MBE system. The solid source materials are placed in effusion cells to provide an angular distribution of atoms or molecules in a beam. The system represents the ultimate in film deposition control, cleanliness, and in situ chemical characterization capability. All of the effusion ovens are mounted in an ultrahigh-vacuum chamber ($\sim 10^{-8}$ Pa). The temperature of each oven is adjusted to give the desired evaporation rate. The substrate holder rotates continuously to improve growth homogeneity.
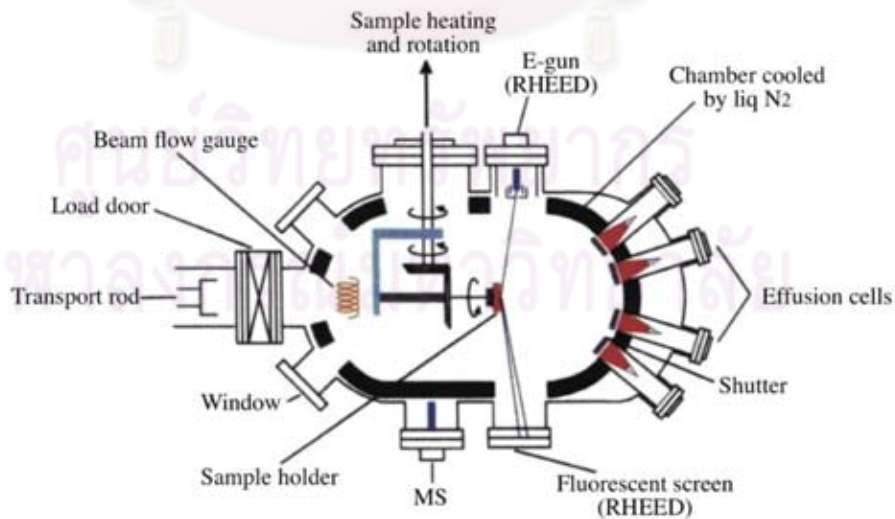
Fig 3.1 Arrangement of the sources and substrate in a typical MBE system.

To grow GaAs, an overpressure of As is maintained, since the sticking coefficient of Ga to GaAs is unity, whereas that for As is zero, unless there is a previously deposited Ga layer.
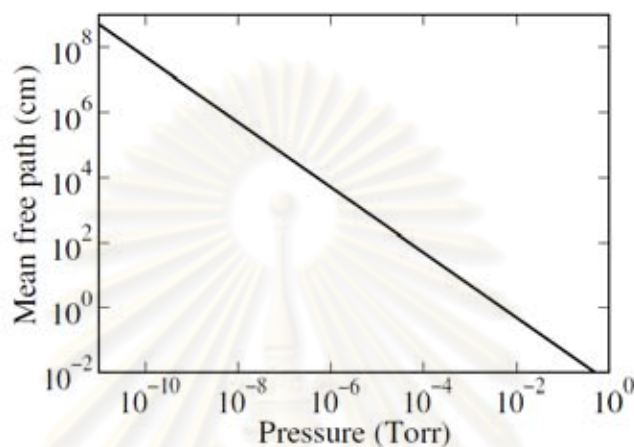
Fig 3.2 Mean free path for nitrogen molecules at 300K.

According to Fig 3.2, the molecular beam condition that the mean free path of the particles should be larger than the geometrical size of the chamber is easily fulfilled if the total pressure does not exceed 10^{-5} Torr. Also, the condition for growing a sufficiently clean epilayer must be satisfied, e.g. requiring for the monolayer deposition times of the beams t_b and the background residual vapor t_{res} the relation $t_{res} < 10^{-5} t_b$. For a typical gallium flux of 10^{19} atom-$m^{-2}s^{-1}$ and for a growth rate in the order of 1 μm/h, the conclusion is that $p_{res} \leq 10^{-11}$ Torr. Considering that the sticking coefficient of gallium on GaAs atoms in normal operating conditions is approximately unity and that the sticking coefficient of most of the typical residual gas species is much less than 1, the condition above results to be not so strict, nevertheless ultra high vacuum (UHV) is required. Thus, UHV is the essential environment for MBE. Therefore, the rate of gas evolution from the materials in the chamber has to be as low as possible. So pyrolytic boron nitride (PBN) is chosen for the crucibles which give low rate of gas evolution and chemical stability up to 1400°C, molybdenum and tantalum are widely used for the shutters, the heaters and other components, and only ultrapure materials are used as source. To reach UHV, a bake-out

of the whole chamber at approximately 200°C for 24 hours is required any time after having vented the system for maintenance. A cryogenic screening around the substrate minimizes spurious fluxes of atoms and molecules from the walls of the chamber. Despite this big technological problems, MBE systems permit the control of composition and doping of the growing structure at monolayer level by changing the nature of the incoming beam just by opening and closing mechanical shutters. The operation time of a shutter of approximately 0.1 s is normally much shorter than the time needed to grow one monolayer (typically 1-5 s). Careful variation of the temperatures of the cells via PID controllers permits the control of the intensity of the flux of every component or dopant of better than 1 %. The UHV environment of the system is also ideal for many in situ characterization tools, like the RHEED (reflection high energy electron diffraction). The oscillation of the RHEED signal exactly corresponds to the time needed to grow a monolayer and the diffraction pattern on the RHEED window gives direct indication over the state of the surface.

MBE uses an evaporation method in a vacuum system. An important parameter for vacuum technology is the molecular impingement rate; that is, how many molecules impinge on a unit area of the substrate per unit time. The impingement rate ($\emptyset$) is a function of the molecular weight, temperature, and pressure. The rate can be expressed as

$$\emptyset = P(2\pi mkT)^{-1/2} \tag{3.1a}$$

or

$$\emptyset = 2.64 \times 10^{20} \left(\frac{P}{\sqrt{MT}}\right) \frac{molecules}{cm^2 \cdot s} \tag{3.1b}$$

Where P is the pressure in Pa, m is the mass of a molecule in kg, k is Boltzmann's constant in J/K, T is the temperature in degrees Kelvin, and M is the molecular weight.

In this work, all samples were grown in a conventional RIBER 32P solid source MBE machine. The MBE machine consists of three chambers, introduction chamber, transfer chamber, and growth chamber. These are separated by isolation gate valves. For introduction chamber, heaters are established for a heat treatment process of the substrate.

Introduction, transfer, and growth chamber are typically maintained in ultra-high vacuum condition by titanium sublimation pumps and an ion pumps. The pressure inside these chambers and beam flux pressure are measured by ion gauges. RHEED and quadrapole mass spectrometer are used to obtain the real time information of growth process and growth chamber conditions.

3.2 Reflection High Energy Electron Diffraction (RHEED)

Reflection high energy electron diffraction (RHEED or R-HEED) is a technique for surface structural analysis. A RHEED system requires an electron gun, electroluminescence detector screen and a sample with a clean surface. The electron gun generates a beam of electrons which strike the sample at very small angle relative to the sample surface. Incident electrons diffract from atoms at the surface of the sample, and a small fraction of the diffracted electrons interfere constructively at specific angles and form regular patterns on the detector. The electrons interfere according to the position of atoms on the sample surface, so the diffraction pattern at the detector is a function of the sample surface. Fig 3.3 shows RHEED schematic.

Because of its small penetration depth, owing to the interaction between incident electrons and atoms, RHEED is primarily sensitive to the atomic structure of the first few planes of a crystal lattice. Therefore, the diffraction from a structure periodic in only two dimensions emphasizes the observed pattern, and the positions of the elastically scattered beams can be computed from single-scattering expressions. Nevertheless, because the elastic scattering is comparable to the inelastic scattering, multiple scattering processes are also crucial, and these must be included to achieve the correct intensity. The RHEED geometry - an incident beam directed at a low angle to the surface - has a very strong effect on both the diffraction and its interpretation. For example, atomic steps can produce large changes in both the measured intensity and the shape of the diffracted beams when the important atomic separations are parallel to the incident beam direction; in contrast, the role of atomic structure in the diffracted intensity is primarily determined by the atomic separations perpendicular to the beam direction. Both of these phenomena result from the low glancing angle of incident. The extent of these sensitivities, the

important of multiple scattering, the shape of the diffraction pattern, and the salient features of calculation are all determined by a combination of the small glancing incident angle and the conservation of parallel momentum.
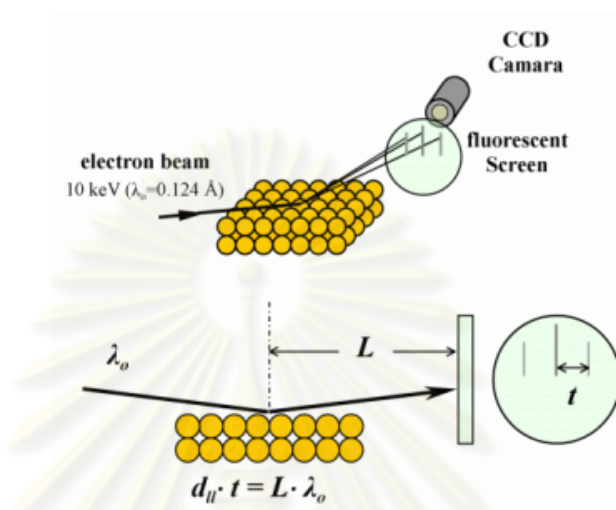
Fig 3.3 Schematic of RHEED.

3.3 RHEED Pattern Observation

The pattern position can be graphically determined by the Laue method – intersection of Edwald sphere in reciprocal lattice space. A schematic representation of the RHEED observation system in the MBE growth chamber is shown in Fig 3.4. Since the short de Broglie wavelength of electron allows a shallow penetration depth into the substrate, only atoms at the sample surface contribute to the RHEED pattern. Diffracted electrons at the flat surface are imaged onto the screen. Therefore, the surface layer is represented by a reciprocal lattice space rod perpendicular to the real surface. If the surface has roughness in the order of an atomic scale, the surface layer in the reciprocal space will be presented by three-dimensional point array. Therefore, we can interpret the RHEED pattern as the reciprocal lattice representation of the sample surface, which reflects the surface morphology on the atomic scale.
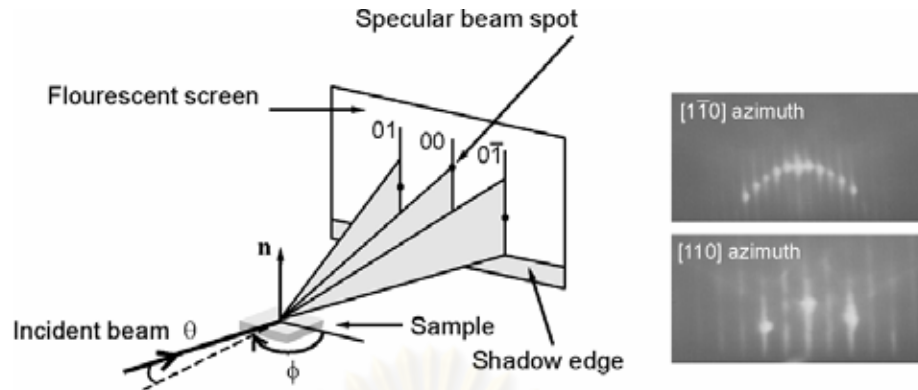
Fig 3.4 Schematic diagram of RHEED geometry showing the incident electron beam at an angle θ to the surface plane. The right part shows diffraction pattern from the GaAs (001) (2×4) surface, in the [1-10] and [110] azimuth.

The condition for imaging on the fluorescent screen is called the *Laue diffraction condition*

$$\boldsymbol{k}_{in} - \boldsymbol{k}_{diff} = \boldsymbol{G} \tag{3.2}$$

where $\boldsymbol{k}_{in}$ and $\boldsymbol{k}_{diff}$ are the wave vectors of the incident and diffracted electrons, respectively, and $\boldsymbol{G}$ is the reciprocal lattice vector. This condition corresponds to Bragg's law in the simple diffraction theory. The pattern position can be graphically determined by the Laue method-intersection of Ewald sphere in reciprocal lattice space.

3.4 RHEED Pattern Oscillation

RHEED intensity oscillation is a typical technique for growth rate determination. This has been also used to calibrate beam fluxes corresponding to the growth rate. To control chemical composition and the thickness of the quantum structures, the fluxes are adjusted to the value corresponding to needed growth rate [26].

The RHEED intensity of the pattern depends on the roughness of the surface. Under the normal growth condition, the RHEED intensity changes according to the fraction of surface coverage where the period of the pattern oscillation corresponds to the growth of 1 monolayer (ML). The schematic representation of the RHEED intensity oscillation is shown in Fig 3.5. In each period, the maximum reflectivity occurs at the initial and final state when the smooth surface was completely grown and the minimum reflectivity occurs at the intermediate state when the growing layer is approximately half completed. With use of the period of oscillation signal, the growth rate of GaAs can be calibrated. The experimental data is shown in Fig 3.6.
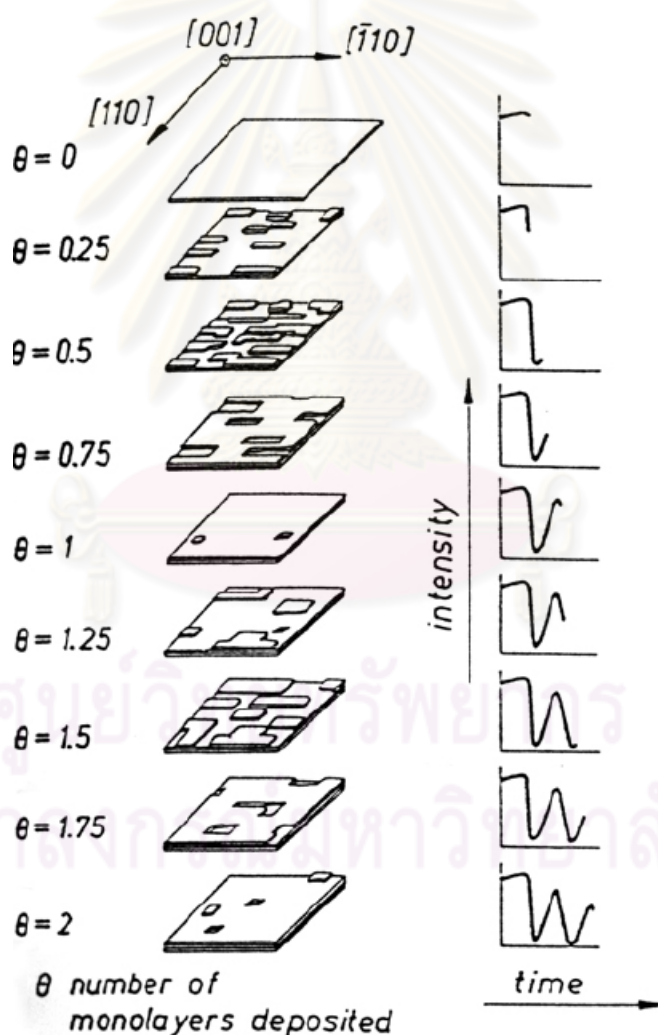
Fig 3.5 Schematic representation of RHEED intensity oscillations related to formation of the first two complete monolayer of GaAs (001).
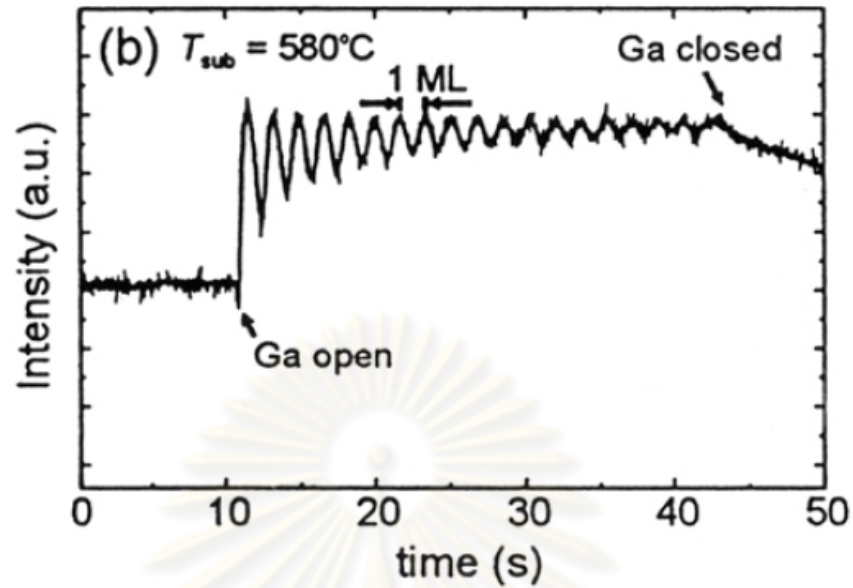
Fig 3.6 RHEED intensity oscillation during the growth of GaAs.

3.5 Atomic Force Microscopy (AFM)

Atomic force microscopy (AFM) is a powerful technique for analyzing and characterizing samples at microscope level. It can be used on both conducting and insulating samples. An AFM measures the force between the tip and the sample, rather than the tunneling current. A sharp tip is mounted on the end of the millimeter-sized cantilever, as shown in Fig. 3.7. A force F exerted on the tip by the sample deflects the cantilever by Δz:

$$F = C\Delta z \,, \qquad (3.2)$$

where C is the force constant of cantilever. The displacement of the cantilever is measured as a function of tip position, often by using the back of the cantilever as a reflector for a laser beam. Motion of the reflector changes the path of the laser beam, which is detected using photodiode array; picometer-scale displacements can easily be measured. Since a typical value of the force constant is $C = 1$ N/m, pN-scale force can be transduced. Forces well below 1 fN have been measured under special circumstances.
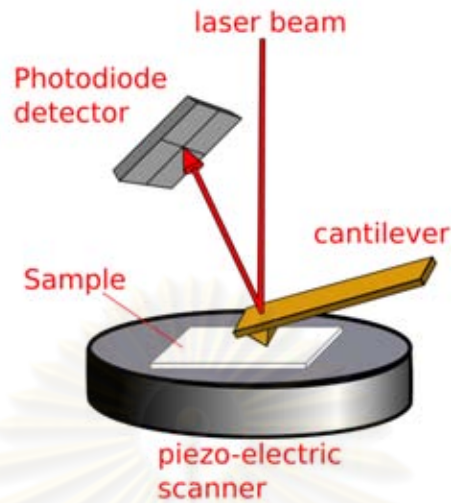
Fig 3.7 Schematic of an atomic force microscope (AFM). Deflections of the
cantilever are measured by a photodetector registering of the position of
a laser beam that reflects of the top of the cantilever.

The simplest mode of operation is contact mode, where the tip is dragged along in
contact with the surface and the cantilever deflection is measured. This gives a measure
of the sample topography, but it can damage the sample. Noncontact or intermittent-
contact imaging modes are less invasive, and they also can give information about the
long-range forces between the sample and the tip. In these techniques, the cantilever
oscillates just above the sample due to an applied driving force of amplitude F_ω near the
cantilever resonance frequency ω_o. Modeling the cantilever as a driven simple harmonic
oscillator, the magnitude of the cantilever response at a frequency ω is given by

$$|z_\omega| = \frac{F_\omega}{C} \frac{\omega_0^2}{\left[(\omega^2 - \omega_0^2)^2 + (\frac{\omega\omega_o}{Q})^2\right]^{1/2}} \tag{3.3}$$

where Q, the quality factor of the oscillator, is the ratio of energy stored in the cantilever
to the energy dissipated per cycle, Note that on-resonance, $\omega = \omega_o$, the response is Q
times larger than at low frequencies, making the detection of small forces possible.

The parameters characterizing the oscillating cantilever are sensitive to any forces, occurring between the tip and the sample. These forces can be Van der Waals, electrostatic, magnetic, or many others. The interaction shifts the resonance frequency ω_o and/or modifies Q. This change is recorded and used to construct an image. For example, in tapping mode imaging, the tip 'taps' the surface during the closest approach of the oscillation cycle, causing both a frequency shift and additional dissipation.

3.6 Photoluminescence (PL) Spectroscopy

Photoluminescence (PL) spectroscopy is employed to characterize the samples in this work. The samples were excited by 476-nm Ar^+ laser. A schematic of the PL experimental setup is shown in Fig 3.8. The laser beam was chopped and focused to the sample by focal lens. The light signal is analyzed by monochromator with a photomultiplier tube. A high-pass filter is used to filter the visible-light noise and the reflected laser beam signal. Then, the resolved light is detected by an InGaAs detector. A chopper and the lock-in amplifier are used to enhance the signal by the standard lock-in technique.
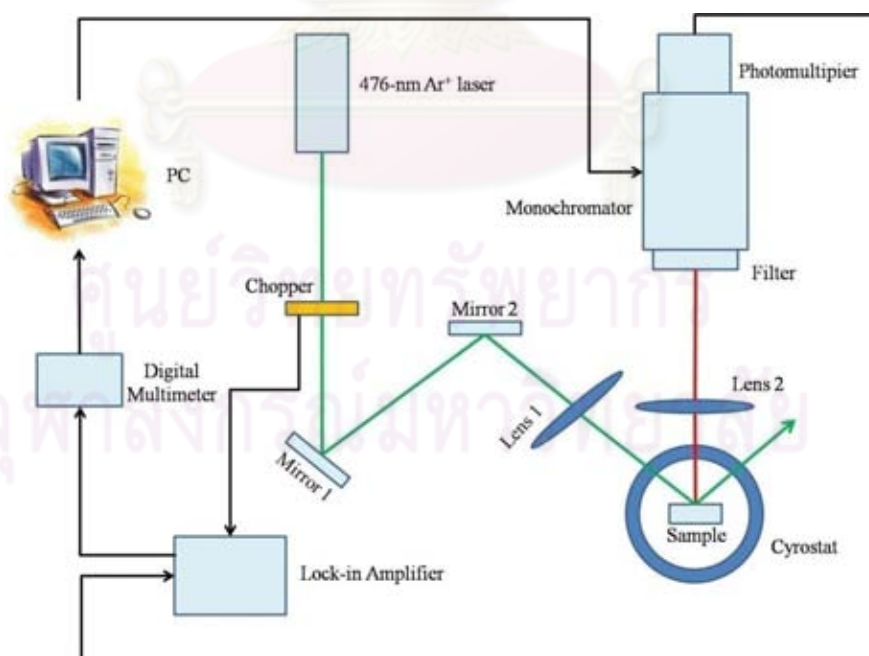
Fig 3.8 Schematic of PL experimental setup.

The interpretation of PL data can simply be described as shown in Fig 3.9 and Fig 3.10. For the case of nanostructures with different size in Fig 3.9, the ground state PL peak energy contains information about the size of the nanosturcture. The increase in nanostructure size results in a lower number of quantized energy levels of both holes and electrons, which causes a lower PL peak energy position. Therefore, this PL peak position can be used to relatively compare the size of nanostructure.

For the shape of PL spectrum from nanostructure array (Fig 3.10), there exists broadening of the spectrum. This broadening, which is measured in terms of a full width at half maximum (FWHM) or PL linewidth, is related to the nanostructure size distribution.
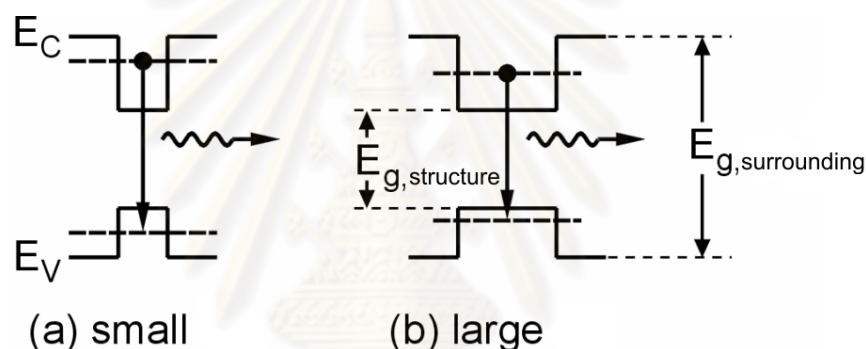
Fig 3.9 Simple interpretation of the PL data obtained from a nanostructure. In case of small-size nanostructure (a) the PL peak energy position is higher compared with large-size nanostructure (b).
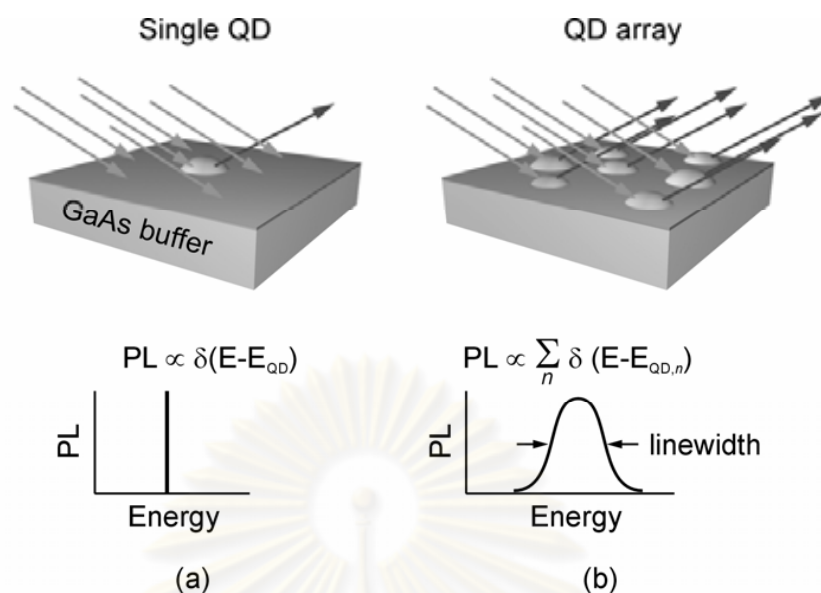
Fig 3.10 Simple interpretation of the PL spectrum obtained from the nanostructure. In (a) the PL spectrum is very narrow due to the delta-function like density of states; and in (b) the *average size* corresponds to the PL *peak* energy position and the PL *line-width* corresponds to the *size distribution* of the array.

3.7 X-ray Diffraction Analysis (XRD)

X-ray diffraction techniques are a family of non-destructive analytical techniques. These techniques reveal the information about crystallographic structure, chemical composition, and physical properties of materials and thin films. XRD techniques are based on observing the scattered intensity of an X-ray beam hitting a sample as a function of incident and scattered angle, polarization, and wavelength or energy.

High resolution X-ray diffraction (HRXRD) is another effective method to study crystal quality, epitaxial composition, layer thicknesses, and relaxations of semiconductors. X-rays, having the photon energy of about 8 keV, penetrate into the sample a depth of max 10 μm. The technique is a non-destructive, fast method to characterize the lattice structure. A schematic layout of the high-resolution diffractometer with optics and specified angles is illustrated in Fig 3.11.
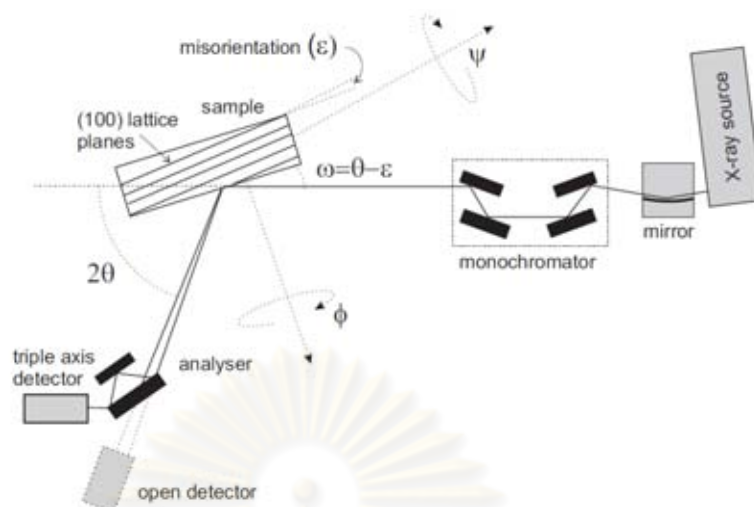
Fig 3.11 Schematic layout of high resolution X-ray diffraction equipment including
relevant components and adjustable angles. The diffraction plane is coincident
with the paper surface.

The highly parallel and monochromatic beam enters the sample at an angle ω, and
the Bragg diffraction angle θ depends on the spacing between the lattice planes. In a two-
axis setup the signal is detected with an open detector using a large acceptance angle of
about $1\circ$ for 2θ. However, because of the large acceptance angle, the open detector is
unable to separate diffuse scattering or small composition deviations. By using an
analyser crystal in front of the detector, the acceptance angle can be reduced to 12 arc
seconds for the 2θ angle [46]. This setup, the triple-axis configuration, also increases the
signal to noise ratio and enables resolution high enough for the reciprocal space mapping
of the samples. Reciprocal, or as presented here, angular space mapping is an effective
method to study samples with tilts between the corresponding lattice planes.

3.8 Transmission Electron Microscopy (TEM)

Transmission Electron Microscopy (TEM) is a microscopy technique in which a
beam of electrons is transmitted through an ultra thin specimen, interacting with the
specimen as it passes through. An image is formed from the interaction of the electrons

transmitted through the specimen; the image is magnified and focused onto an imaging device, such as a fluorescent screen, on a layer of photographic film, or to be detected by a sensor such as a CCD camera.

TEMs are capable of imaging at a significantly higher resolution than light microscopes, owing to the small de Broglie wavelength of electrons. This enables the instrument's user to examine fine detail—even as small as a single column of atoms, which is tens of thousands times smaller than the smallest resolvable object in a light microscope. TEM forms a major analysis method in a range of scientific fields, in both physical and biological sciences. TEMs find application in cancer research, virology, materials science as well as pollution and semiconductor research. The example of TEM image is shown on Fig 3.12.
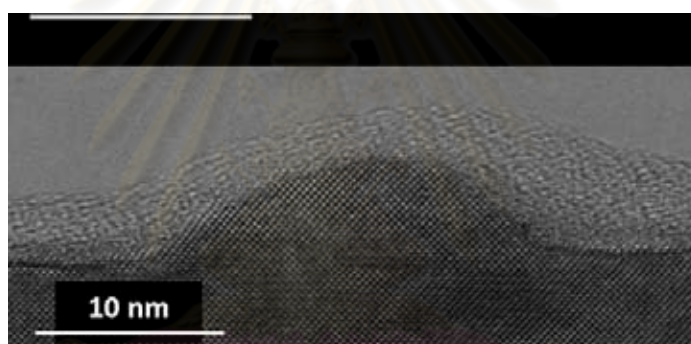
Fig 3.12 TEM image of a quantum dot on a gallium arsenide layer. On top is a glue layer due to TEM preparation only [University of Sheffield].

3.9 Spectral Response Measurement

The spectral response is conceptually similar to the quantum efficiency. The quantum efficiency gives the number of electrons output by the solar cell compared to the number of photons incident on the device, while the spectral response is the ratio of the current generated by the solar cell to the power incident on the solar cell. A spectral response curve of silicon solar cells under glass is shown in Fig 3.13. At short wavelengths below 400 nm the glass absorbs most of the light and the cell response is very low. At intermediate wavelengths, the cell approaches the ideal. At long

wavelengths, the response decreases to zero. Silicon is an indirect band gap semiconductor therefore there is not a sharp cut off at the wavelength corresponding to the band gap (E_g = 1.12 eV).
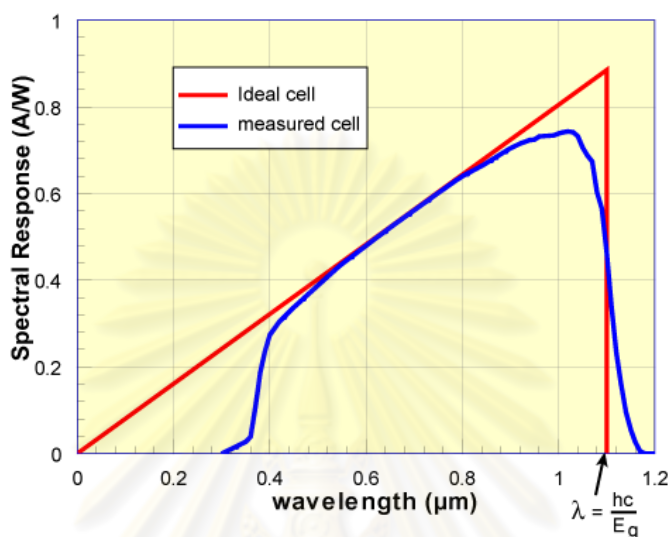
Fig 3.13 The spectral response of a silicon solar cell under glass.

The ideal spectral response is limited at long wavelengths by the inability of the semiconductor to absorb photons with energies below the band gap. This limit is the same as that encountered in quantum efficiency curves. However, unlike the square shape of QE curves, the spectral response decreases at small photon wavelengths. At these wavelengths, each photon has a large energy, and hence the ratio of photons to power is reduced. Any energy above the band gap energy is not utilized by the solar cell and instead goes to heating the solar cell. The inability to fully utilize the incident energy at high energy, and the inability to absorb low energies of light represents a significant power loss in solar cells consisting of a single p-n junction. In our work, spectral response measurement setup is illustrated in Fig 3.14. A white light source (halogen lamp) is chopped and is passed through 1000M SPEX monochromator for the selective wavelengths. The selected wavelengths are scanned on the samples for their photoconductive signals which are connected to a lock-in amplifier and to a computed displaying the spectral response curves.
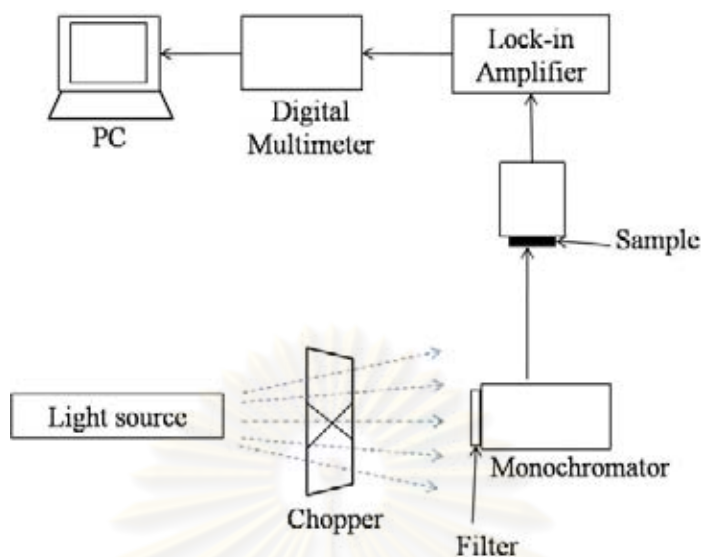
Fig 3.14 Schematic of spectral response setup.

3.10 Sample Preparation

In this work, all samples were fabricated by MBE technique using RIBER 32P molecular-beam epitaxy-system. The detailed sequences for sample preparation are as follows.

(1) Pre-heated process : a piece of (001) Ge substrate was glued on a Mo (Molybdenum) by using indium glue. The block with the substrate was transferred to the introduction chamber and heated to 450°C for 60 minutes in order to eliminate water (H_2O) and oxide from the substrate.

(2) De-oxidation (removing oxide from substrate surface) : After preheated process, the sample (the substrate on Mo block) was transferred into the growth chamber. Then, the substrate temperature was increased to 620°C. This temperature was maintained for 20 minutes in order to remove the native oxide from the surface. RHEED pattern is shown in Fig 3.15.
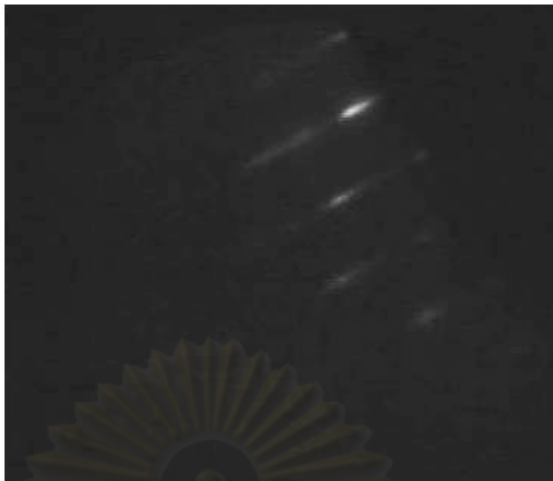
Fig 3.15 RHEED pattern observed during the de-oxidation process.

(3) Growth of AlAs interfacial layer by MEE technique : After the oxide removal
     at 620°C, the substrate temperature was decreased and a 30-nm AlAs was
     grown at 350°C using MEE technique. The AlAs growth rate was about 0.1
     monolayers/second (0.1 ML/s). RHEED pattern during this process is shown
     in Fig 3.16.

Fig 3.16 Spotty RHEED pattern observed during MEE-AlAs growth.

(4) Growth of GaAs by MEE technique : After AlAs layer was grown at $350^{\circ}C$, GaAs layer was grown at this temperature by MEE technique. The cycle of the MEE growth consisted of 2 s in which the As shutter was open (Ga closed), 2 s in which the Ga shutter was open (As closed) and 1 s for interrupted time (As and Ga closed). As_4 species with a flux of 4×10^{-6} Torr and 0.1 ML/s GaAs growth rate were used throughout this process. The MEE consisted of 100 monolayers (~ 30 nm) of GaAs. RHEED pattern of 30 nm-GaAs grown by MEE technique is shown in Fig 3.17.

Fig 3.17 RHEED pattern of 30 nm-GaAs grown by MEE technique.

(5) A two step GaAs nucleation process : Firstly, the initial 100 nm of GaAs was deposited at $350^{\circ}C$ under As_4 flux of 5×10^{-6} Torr by using a slow GaAs growth rate of 0.1 ML/s. Secondly, the subsequent growth was conducted at this temperature with GaAs growth rate of 0.5 ML/s under As_4 flux of 8×10^{-6} Torr. GaAs thickness was varied at this step. MEE and conventional growth technique were used for this process. RHEED pattern of 1 µm-GaAs is shown in Fig 3.18.
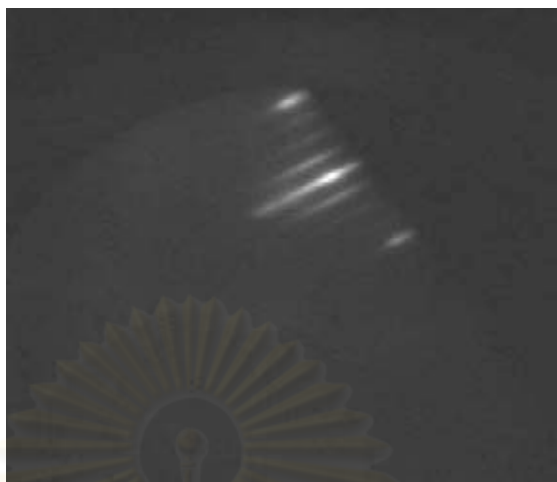
Fig 3.18 Streaky (2×4) RHEED pattern of GaAs surface observed after the
formation of 1 µm-GaAs buffer layer.

(6) Self-assembled InAs QDs nucleation process : After the two step GaAs
nucleation process was finished, the substrate temperature was ramped up to
500°C and InAs QDs were grown with InAs coverage of 1.8 MLs. RHEED
pattern of InAs QDs grown on GaAs/AlAs/Ge substrate is shown in Fig 3.19.

Fig 3.19 RHEED pattern of InAs QDs grown on GaAs/AlAs/Ge substrate.

(7) For photoluminescence (PL) measurements, the samples were capped with GaAs, AlGaAs, and GaAs at 510°C with thicknesses of 50, 60, and 50 nm, respectively.

CHAPTER IV

RESULTS AND DISCUSSIONS

In t his c hapter, t he e xperimental r esults of G aAs g rown on G e s ubstrates, including s elf-assembled InAs qua ntum dot s on a nti-phase dom ains of G aAs on G e substrates, are di scussed. T he A PDs and APBs o f G aAs have be en obs erved. W e ha ve varied the t hickness of G aAs. B y us ing a tomic force m icroscopy (AFM), the e ffects of the GaAs thickness on the size of the APDs can be investigated. The GaAs/p-Ge schottky devices and p-n j unction de vices a re fabricated. I-V ch aracterictics of t hese de vices are revealed. TEM and XRD results indicate the crystal imperfection of GaAs epitaxial layer, i.e. di slocations a nd s tacking f aults. S pectral r esponse of G aAs grown on A lAs/Ge substrated i s i nvestigated. P L r esults of G aAs grown on Ge s ubatrates ar e pr esented. These i ndicate a tomic i nterdiffusion be tween G aAs l ayer a nd G e s ubstrate. M oreover, self-assembled InAs Q Ds g rown on G e s ubstrates a re i nvestigated b y u sing A FM and also PL measurement.

4.1 Surface Morphology : AFM

4.1.1 Anti-Phase Domains (APDs) Investigation

For s tructural ch aracterization, the surface m orphology of t he s amples af ter crystallization under As_4 flux (sequence (4) i n s ection 3.8) w as inve stigated by tapping-mode at omic force m icroscope (AFM) i n air. The ant i-phase dom ains (APDs) of GaAs have be en obs erved. A FM i mage of A PD-GaAs g rown on p -Ge b y c onventional M BE technique i s s hown on Fig 4.1. A s de scribe above, A PDs r esult f rom the i nteraction between polar and non-polar compound semiconductor. From Fig 4.1, the APDs look like a m at texture. A lso, t hese de fects i ntroduce p erformance reduction m echanisms a nd significant s urface r oughness. The ef fect of i nitial G e s urface ex posure, in this cas e between G a a nd A s exposure, ha s be en investigated in t he pa st us ing s everal growth techniques, with apparently contradictory experimental results [47-48]. S.A. Ringel

and R.M. Sieg have used both As and Ga to initiate the MEE, and have obtained defect-free material using either approach [1]. Because Ga has self-terminating property, the growth initiation via a Ga exposure requires calibration of the deposition rate to ensure a single complete Ga monolayer is deposited. In contrast, As is self-terminating on Ge at temperature of 350°C or higher, therefore precise As flux control is not required. The nucleation without the MEE, i.e. nucleation by brief As exposure at 500°C followed by opening the Ga shutter to initiate coevaporation, also produced nearly APD-free material. However, the prolonged As exposure at high temperature was observed to degrade the interface quality by generating some APDs [49]. In this work, we have grown GaAs by using both As and Ga prelayer to initiate the MEE. AFM images of GaAs grown by MEE with As and Ga prelayer are shown on Fig 4.2.
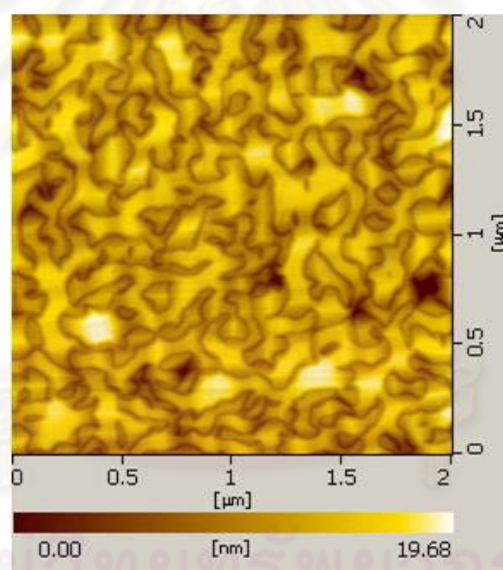
Fig 4.1 AFM image of APD-GaAs grown on p-Ge by conventional MBE technique. GaAs thickness is about 100 nm.

<div style="text-align:center">(a)   (b)</div>
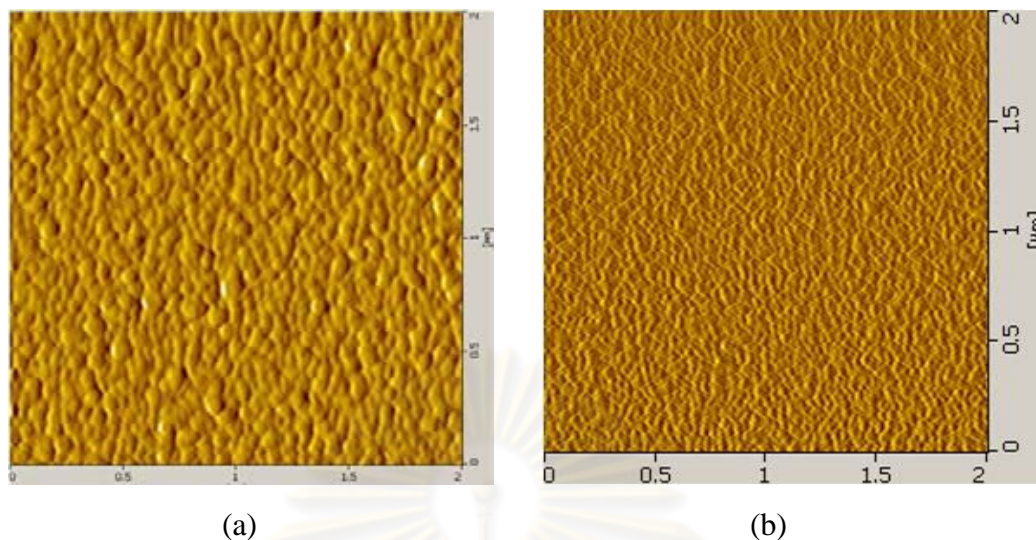
Fig 4.2 AFM images of GaAs grown on p-Ge by MEE technique using (a) As prelayer, (b) Ga prelayer. GaAs thickness is 30 nm.

Growth of the epitaxial Ge layer with thickness of 100 nm was found to be critical to produce a smooth, chemically clean starting surface as verified by S.A. Ringel and R. M. Sieg. The nucleation of GaAs directly on the Ge surface (without any epitaxial Ge growth) typically resulted in high defect densities due to the uncontrolled initial surface [1]. However, Ge cell has not been installed in our MBE machine, therefore GaAs was inevitably grown directly on the Ge substrate.

The growth of GaAs on Ge substrate cover with a layer of GaAs is quite similar to the growth of GaAs on GaAs substrate. Thus the growth rate as well as the substrate temperature can be increased after sufficient has elapsed to ensure enough nucleation to cover the entire Ge surface with GaAs epilayer. This growth initiation at low temperature and subsequent increase to a higher (normal) growth temperature is often referred to the two step growth process [50]. A number of studies have been carried out to relate the choice of initial temperature to the quality of the initial (buffer) epilayer [51-53]. Good surface morphology can be achieved at low growth temperature of around $250^{o}C$. However, the quality of the initial buffer layer is not good at this temperature. As the initial temperature is increased, the surface morphology is degraded, tending towards white cloudiness of the surface [54]. In our experiment, some samples exhibit this

condition as shown in Fig 4.3. However with increase in temperature, the quality of initial GaAs epilayer improves. When the second step of the two step growth process is initiated, the higher growth temperature affects the initial buffer layer, i.e. the quality of the initial buffer layer is improved by annealing effect because of subsequent high temperature growth. This is due to the annealing of microtwins, but the threading dislocations are generated in this process as studied by C. W. Nieh et al.
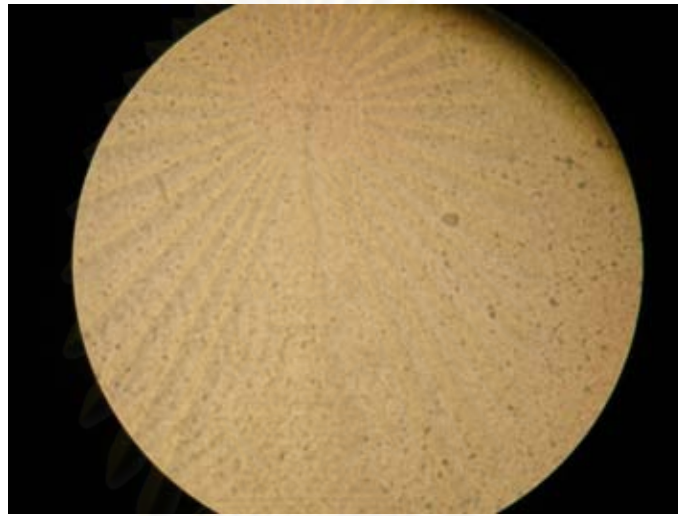
Fig 4.3 Image of white cloudiness surface resulting from excessive growth temperature.

Substrate annealing at high temperature, coupled with the large offcut substrate, results in a double-stepped Ge surface as confirmed by J. M. Zhou et al [55]. AFM images of GaAs grown on 6° offcut Ge/Si substrate and on p-Ge oriented substrate are shown on Fig 4.4. From Fig 4.4, the depth of domain boundary of GaAs on p-Ge is little smaller than depth of domain boundary of GaAs on 6° offcut Ge/Si substrate. Moreover, if we consider the AFM images on the larger scale, the surface of the sample in Fig 4.4 (d) tends to be smoother than the one in Fig 4.4 (c). In order to reduce cost and the fact that oriented Ge (001) is practically used, we choose oriented Ge (001) substrate in our experiment.

(a)   (b)

(c)   (d)
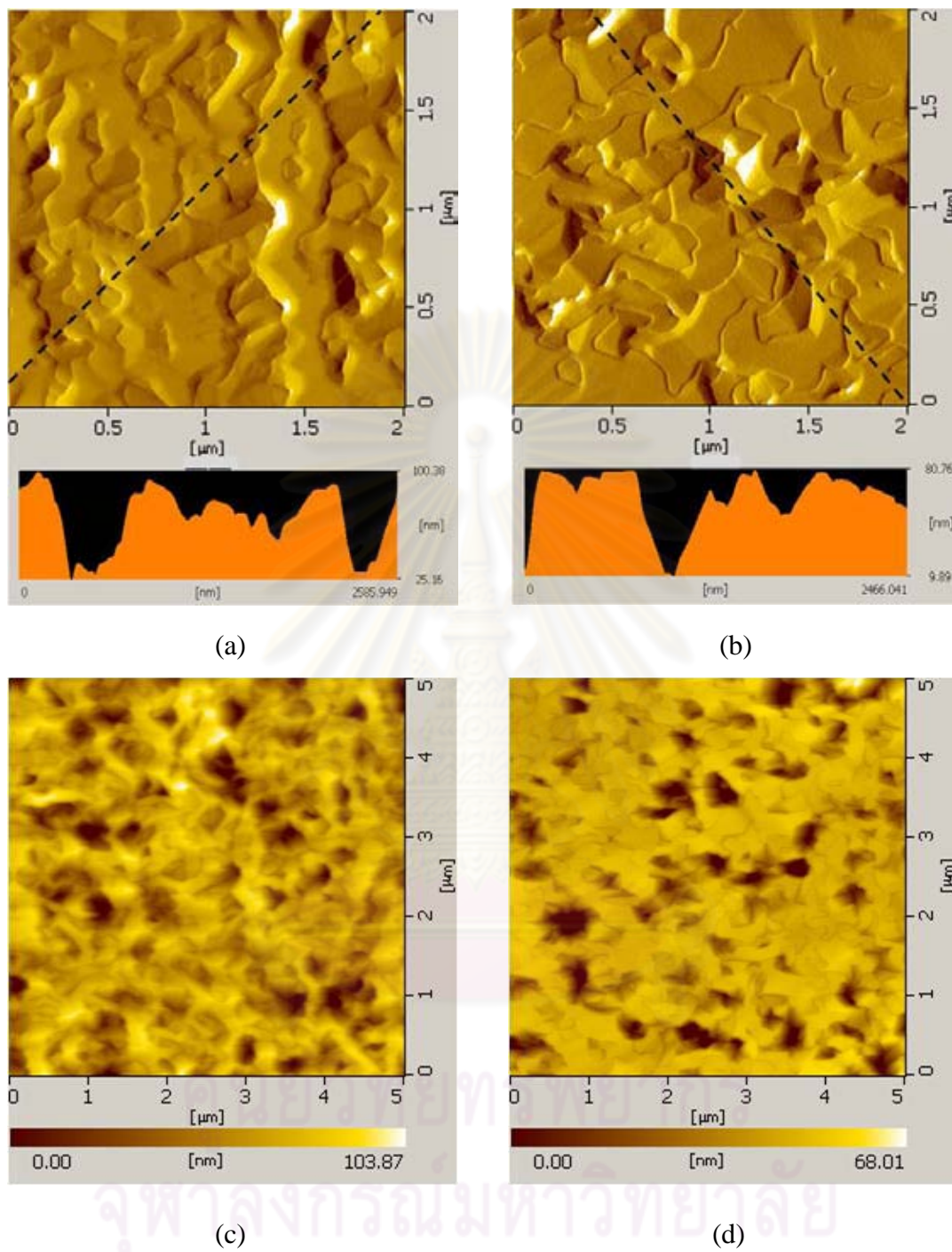
Fig 4.4 AFM images of GaAs grown on 6° offcut Ge/Si substrate ((a) and (c)) and on
p-Ge oriented substrate ((b) and (d)). The total thickness of GaAs epilayer
is about 80 nm on both types of substrate.

Fig 4.5 and 4.6 show the atomic force microscope (AFM) images of GaAs surface with thicknesses of 500 nm and 1 μm on p-and n-Ge whereas Fig 4.7 shows their corresponding structure. The AFM images show many of anti-phase domains (APDs) which result in anti-phase boundaries (APBs). The average domain size of the samples in the Fig 4.6 is larger than Fig 4.5 about 2 times and the depth of the domain boundaries is in the range of 10-40 nm for both Fig 4.5 and 4.6. As a result, it can be seen that the domain size varies with the GaAs thickness. However, the GaAs thickness should be optimized to providing the suitable domain size for a good TANDEM solar cell.

(a)   (b)
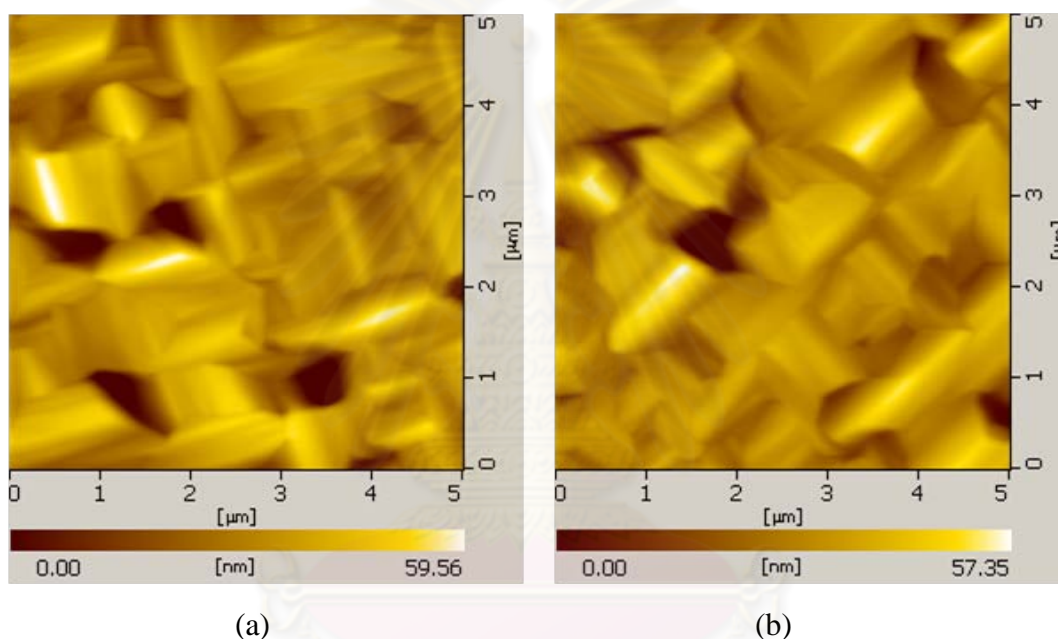
Fig 4.5 AFM images of 500 nm-GaAs surface on p-Ge (a) and n-Ge substrates (b).

(a)   (b)
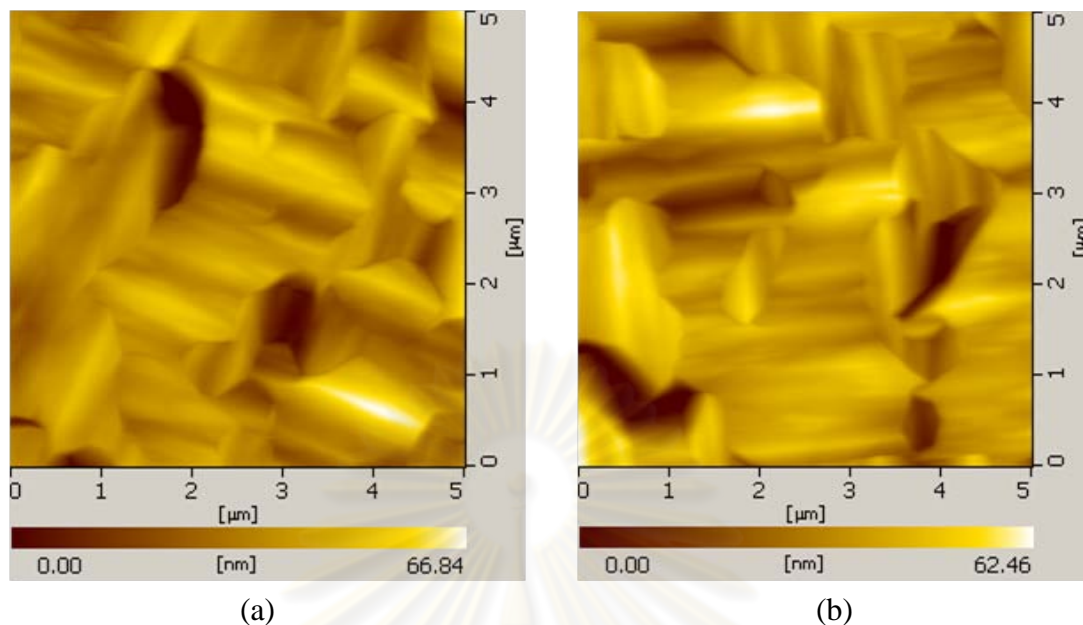
Fig 4.6 AFM images of APD-GaAs surface with thickness of 1 μm on p-Ge (a) and n-Ge substrates (b).
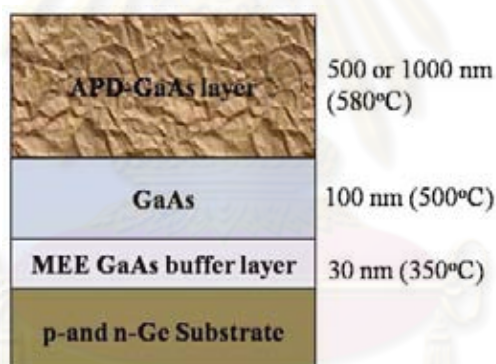
Fig 4.7 Structure of the samples in Fig 4.5 and 4.6.

In order to improve the junction quality both anti-phase domains should be eliminated and gold diffusion should be stopped by some blockage layer like AlAs which is proved to be effective in decreasing interdiffusion between Ge and GaAs [56- 57]. An introduction of large bandgap AlAs to the sample structure gives also heteroface which is desirable for some other photonic devices like waveguides and emitting devices. It is confirmed by AFM image as shown in Fig 4.8 that anti-phase domains still exist in AlAs epitaxial layer grown on (001) Ge substrate. However, we have grown GaAs on AlAs interfacial layer. AFM image of GaAs grown on AlAs/Ge is shown in Fig 4.9.
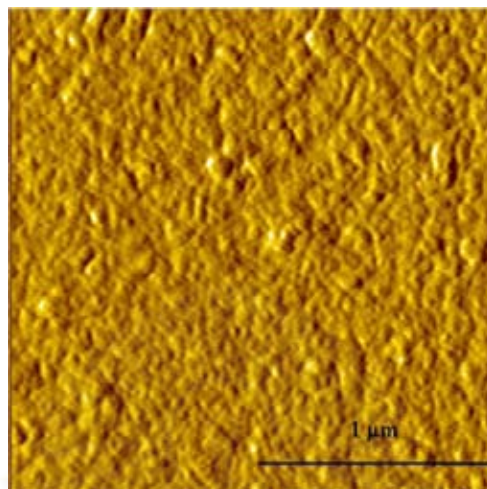
Fig 4.8 AFM image of AlAs surface grown by MEE technique with AlAs thickness of
100 ML (~30 nm).
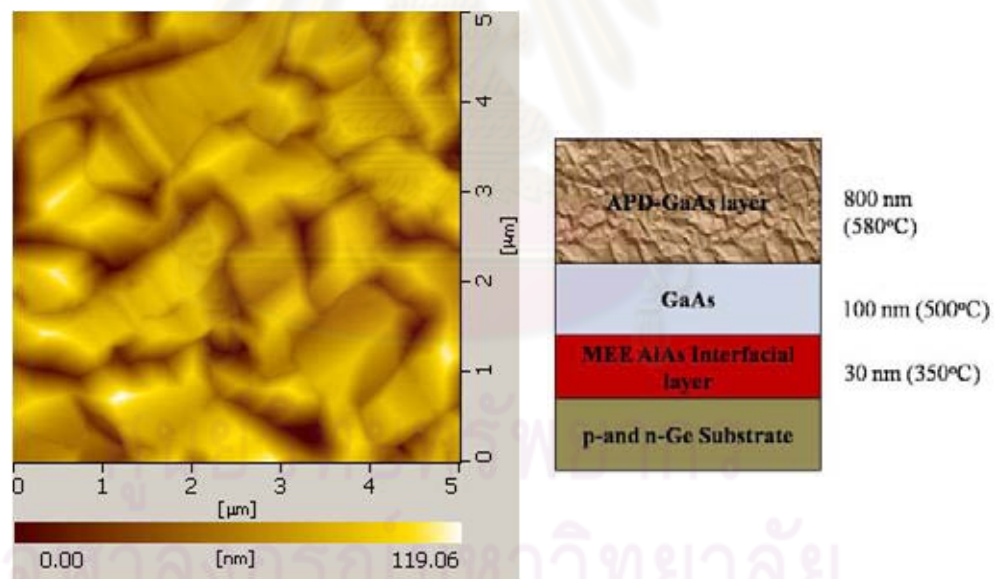
Fig 4.9 AFM image of GaAs grown on AlAs/Ge and its corresponding structure.
Thickness of APD-GaAs layer is about 800 nm.

4.1.2 Self-Assembled InAs QDs on APDs

QDs growth temperature and InAs coverage were fixed at $500^{o}C$ and 1.8 MLs at InAs growth rate of 0.01 ML/s. We use standard Stranski-Krastanov (SK) growth mode in which In and As shutters are simultaneously opened so there is a wetting layer (WL). Due to the high elastic potential energy, once certain critical thickness is achieved, additional atoms group together to form the quantum dot to reduce this elastic energy. The WL thickness is roughly 0.5 nm. Because of GaAs atoms placing on the wrong site resulting in APDs, the strain field significantly occurs around these APBs. This consequently impact on the WL of InAs. Before the InAs WL was nucleated, there has been the residual strain field inside GaAs, especially around the APBs. Thus, the WL critical thickness formed on APDs-GaAs is probably smaller than the WL critical thickness formed on GaAs without APDs. Fig 4.10 shows the AFM images of InAs QDs grown on (a) 300-nm and (b) 700-nm GaAs/AlAs/Ge. Histograms of QD height distribution are also included in Fig 4.9.

In SK growth mode, few monolayers of two- dimensional (2-D) growth appear prior to QD formation. The critical layer thickness at which this 2-D to 3-D transition occurs depends on the lattice mismatch between the layer being deposited and the GaAs buffer layer. For InAs layer on GaAs substrate, the critical layer thickness is around 1.6 MLs. As we increase deposition thickness to 1.8 MLs which is above the critical thickness, QDs formation was observed, as shown in Fig 4.10. Owing to anisotropic property of QDs, elliptical quantum dots occur. Fig 4.11 shows the cross-sectional profiles of QD.

53
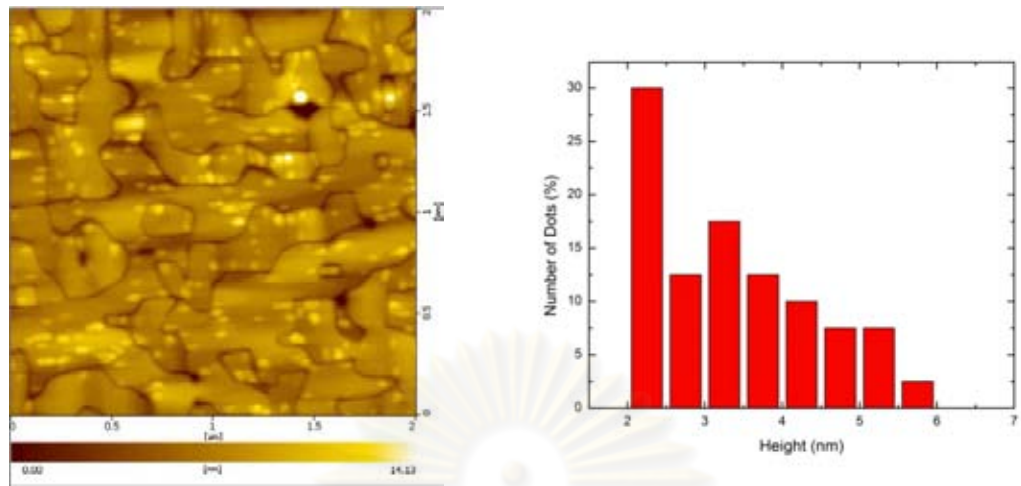
(a)
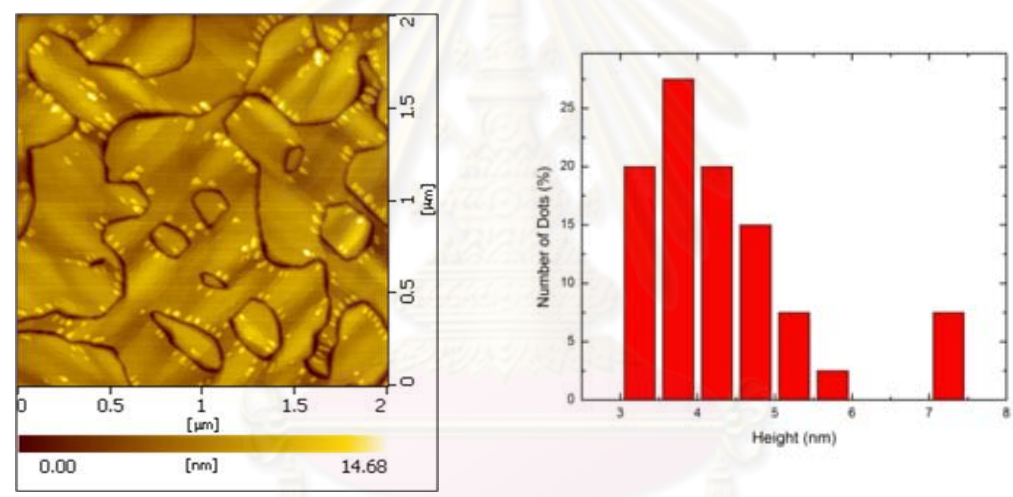
(b)
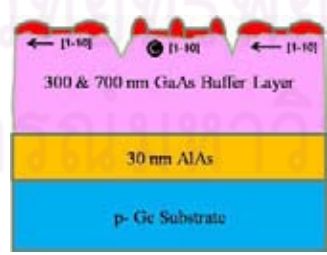
(c)

Fig 4.10 AFM images of QDs grown on different GaAs thickness of (a) 300 nm and (b) 700 nm. Its histogram of QD height distribution is on the right of each AFM image. Their corresponding structure is also included in (c).
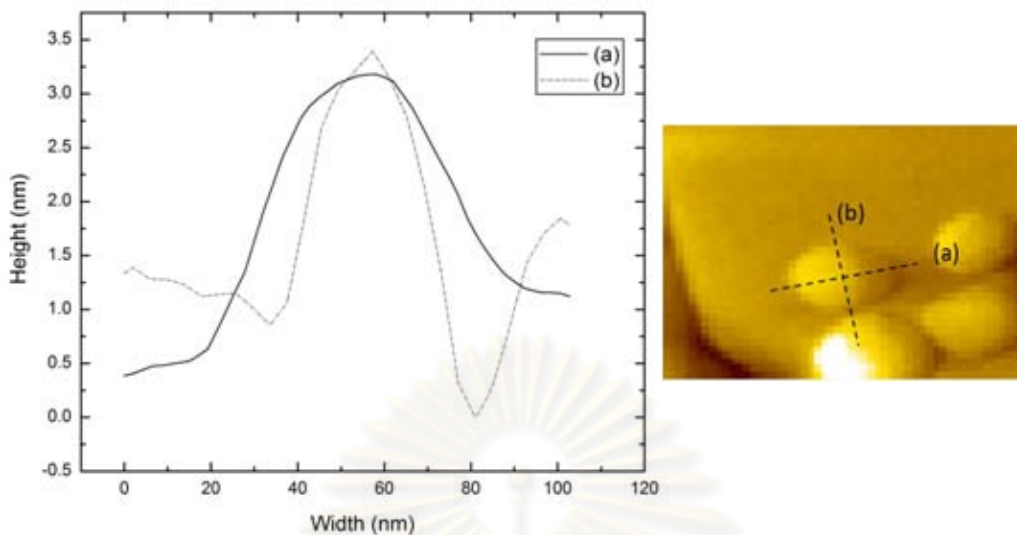
Fig 4.11 Cross-sectional profiles of QD.

The sample with GaAs thickness of 300 nm show the size distribution of InAs dots having a length of major axis, minor axis and average height of 76.4 nm $\pm$ 10 %, 48.4nm $\pm$ 8 %, and 3.2 nm $\pm$ 1 % and the sample with GaAs thickness of 700 nm show the size distribution of InAs dots having a length of major axis, minor axis and average height of 64.8 nm $\pm$ 10 %, 37.9 nm $\pm$ 5 % and 4.2 nm $\pm$ 1 %, respectively. Dot density, determined from the AFM images of Fig 4.10, with GaAs thickness of 300 and 700 nm are 4.8×10^9 cm^{-2} and 5×10^9 cm^{-2}, respectively. The elongated dots align in a specific direction. Especially, in the case of large domain size, as shown in the Fig 4.10 (b), most of InAs quantum dots align in the direction normal to the boundary of APDs or APB and also to elongated quantum dot alignment formed in the adjacent domain. Each domain has only one specific crystallographic direction of the QDs elongation, as proved to be $[1\bar{1}0]$ direction by Suraprapapich et al [58]. The orientation of GaAs zinc-blende structure and the single-step surface of (001) Ge [59] affect the strain field inside GaAs layer. Thus, QDs prefer to accumulate in the region possessing high strain field which is the region near the APBs. This high strain field results from atoms placing on the wrong site. However, QDs are always aligned along $[1\bar{1}0]$ but, the $[1\bar{1}0]$ changes between the main phase and the other phase. The changing of domain orientation is the result of double domain reconstructed surfaces of (001) Ge [59]. The single steps on (001) Ge

without miscut lead to double domain reconstructed surfaces of (001) Ge and also affect the GaAs domain orientation. The orientation of dimer bond of Ge atom on the single-step surface rotates 90° in each domain. As a result, the orientation of GaAs sublattice in each domain is also rotated by 90°. We can use this elongated QDs alignment as indicator for crystallographic formation of each GaAs APDs. For clarity, the larger scale AFM images of QDs grown on different GaAs thickness of 300 nm and 700 nm are shown in Fig 4.12.

(a)   (b)
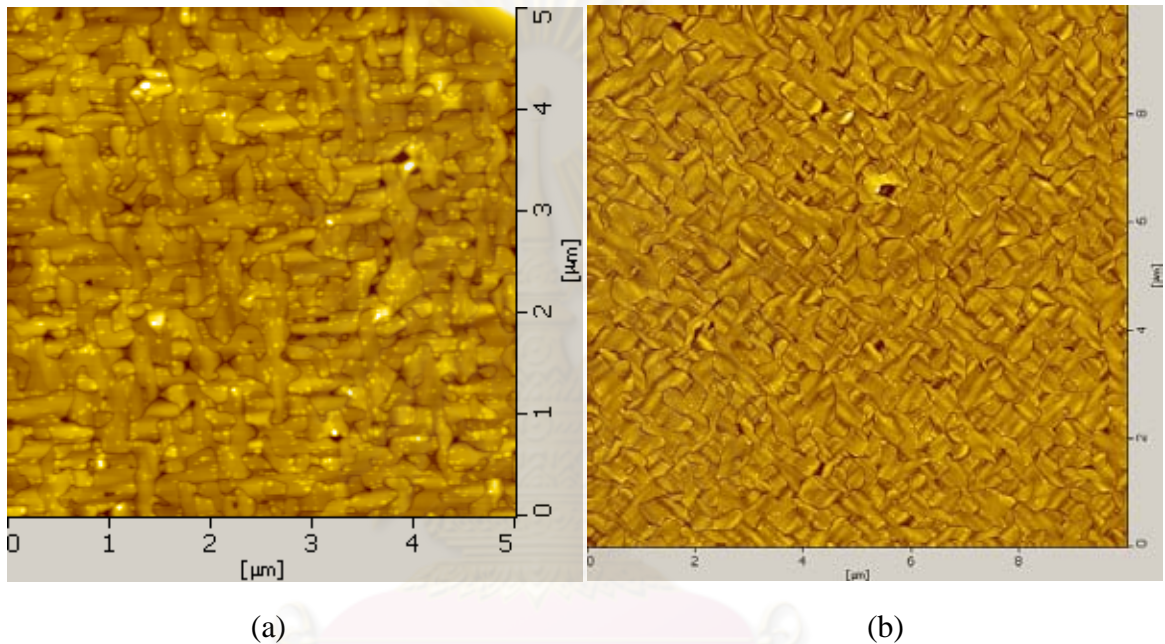
Fig 4.12 The larger scale AFM images of QDs grown on different GaAs thickness of (a) 300 nm and (b) 700 nm.

4.2 Determination of Crystal Imperfection by TEM

To determine the crystal imperfection of the sample, we employed TEM method. Fig 4.13 shows the cross-sectional transmission electron microscope (TEM) images of 1 µm-GaAs film which contain threading dislocations and APDs. This is due to the uncontrolled initial Ge surface as described by S.A. Ringel and R.M. Sieg [1]. These images are representative of numerous regions which were sampled by TEM imaging. The propagation of APDs, stacking faults, and dislocations start at the GaAs/Ge interface but a lot of them terminate before reaching the surface.
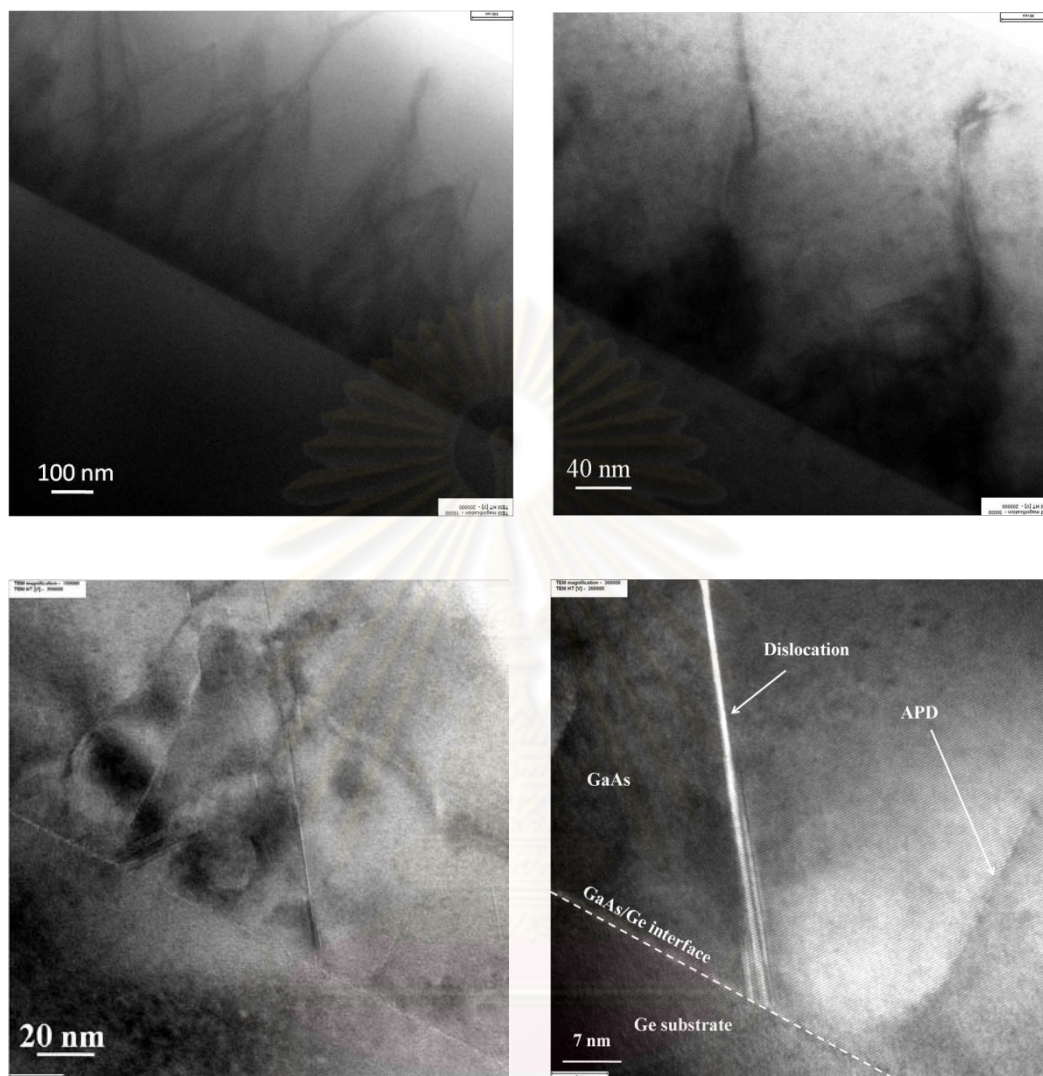
Fig 4.13 TEM images of 1 µm-GaAs on Ge substrate at various scale sizes.

4.3 Crystalline Quality : XRD

XRD method was used in order to determine the crystalline quality. Fig 4.14 shows the XRD result of 1µm-GaAs on 30 nm-AlAs/p-Ge substrate. As seen from this figure, GaAs curve is superimposed on Ge curve. Moreover, there are no fringes from this measured curve indicating imperfect crystal structure and low-quality interface between GaAs epilayer and Ge substrate. This is due to many dislocations and APDs inside the GaAs epilayer.
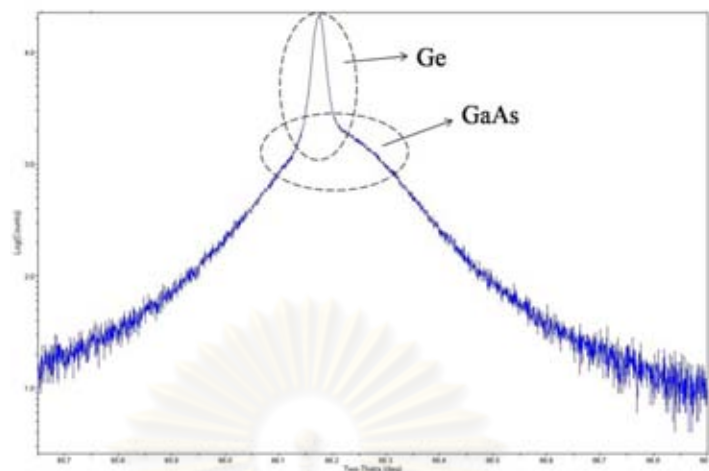
Fig 4.14 XRD result of 1 µm-GaAs on 30 nm-AlAs/p-Ge substrate.

4.4 Electrical Property : Current-Voltage (I-V) Characteristics

4.4.1 Experimental Result on GaAs/Ge Schottky Devices and Discussion

The schematic structure of GaAs/Ge Schottky device is illustrated in Fig 4.15. It consists of a p-Ge substrate, MEE GaAs buffer layer (30 nm), a 100 nm GaAs layer grown at 500°C and either 500 nm or 1 µm GaAs layers grown at 580°C. Schottky contact to the GaAs and Ohmic contact to p-Ge are made with gold and indium evaporation, respectively.
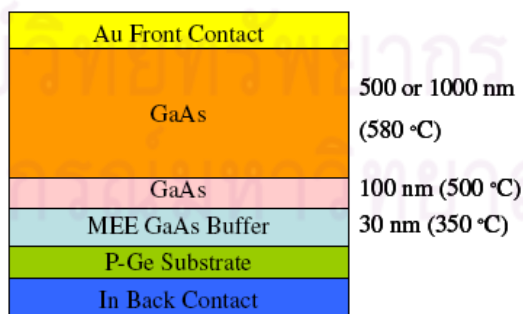
Fig 4.15 Schematic structure of GaAs/Ge Schottky device.

The GaAs/p-Ge Schottky devices with GaAs thickness of 500 nm and 1 µm exhibit current-voltage (I-V) characteristics as shown in Fig 4.16. From Fig 4.16 (a) and

(b), nearly symmetrical I-V curve on both forward and reverse bias indicate that leaky rectifying junctions exist. Expected Schottky junction at Au/GaAs interface leaks along the anti-phase boundaries (APBs). One reasonable explanation for this phenomenon is that when gold is evaporated to form a front contact, because of its high diffusion coefficient, gold atoms can diffuse through the depth of the domain boundaries in GaAs and reach p-Ge substrate therefore resulting in poor junction.

(a)   (b)
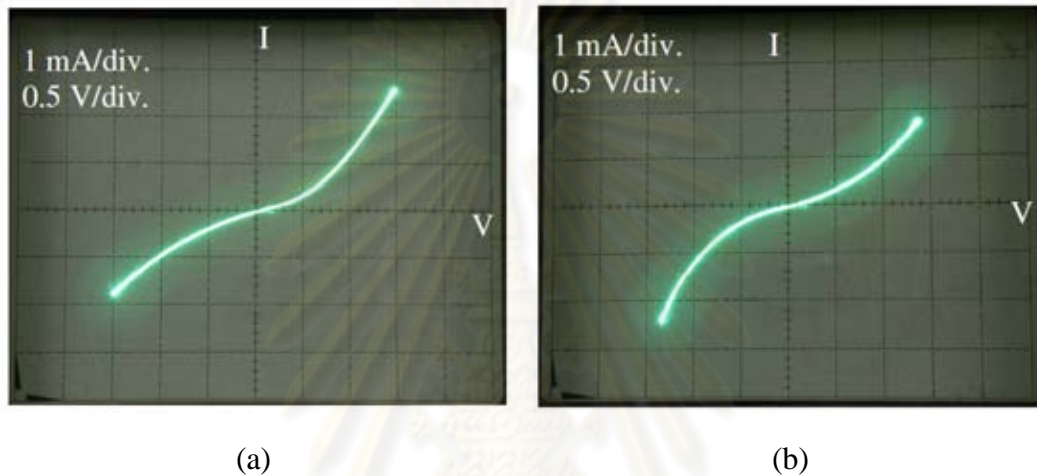
Fig 4.16 Current-voltage characteristics of GaAs/p-Ge Schottky devices with 500 nm (a) and 1 μm (b) GaAs epitaxial layers.

4.4.2 Experimental Result on n-GaAs/n-AlAs/p-Ge p-n Junction

The Ohmic contact structure is shown in Fig 4.17. N. Chand et al. have proposed that introducing AlAs as an interfacial layer is proved to be effective in decreasing the interdiffusion between Ge and GaAs. Therefore, in our work, the MEE-GaAs layer is replaced by AlAs blocking layer. Also, this results in heterointerface which can absorb wide-range energy spectrum. Ohmic contact to n-GaAs and p-Ge are made with Au/Ge/Ni and In evaporation, respectively.
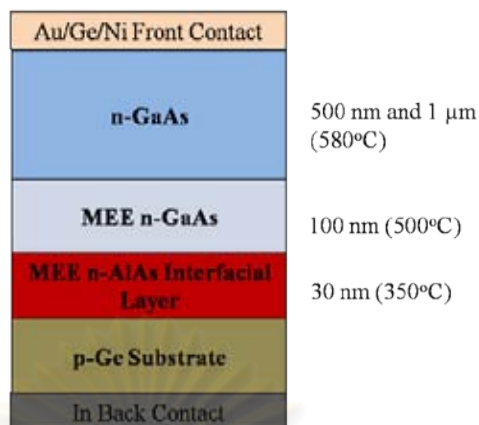
Fig 4.17 Schematic structure of p-n junction devices.

The p-n junction devices with GaAs layers of 500 nm and 1 μm show current-voltage (I-V) characteristics as revealed in Fig 4.18. From Fig 4.18 (a) and (b), the first quadrant refers to the forward bias condition, while the third quadrant refers to reverse bias. On both figures, the cut-in voltage is about 0.7 V. The current flowing through them is initially small until a certain voltage is reached then the current begins to increase rapidly to a large value in the order of a milliampere. If we consider in the third quadrant of both figures, the leakage current can be seen. As a result, this indicates that the junction quality is little improved. Because of the existence of APDs, as seen from Fig 4.9, the junction quality is inevitably limited.

(a)   (b)
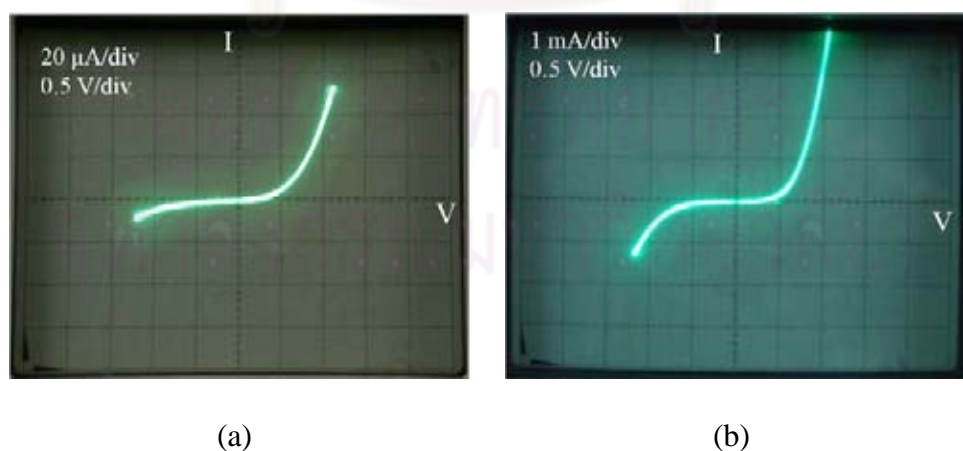
Fig 4.18 Current-voltage characteristics of n-GaAs/n-AlAs/p-Ge p-n junction devices
with 500 nm (a) and 1 μm (b) GaAs epitaxial layers.

When the junction is illuminated, light or photon creates electron-hole pairs in *p*, *n*, and depletion region. Carrier concentration *n* and *p* are then enhanced above their equilibrium values, and the electron and hole quasi Fermi levels are split. I-V characteristic of device structure in Fig 4.17 with GaAs thickness of 500 nm under the light illumination is shown in Fig 4.19. I-V curve in the dark is also included in Fig 4.19 for comparison. This figure represents the third quadrant of the I-V curve in the Fig 4.18. The light source is halogen lamp. As a result, the device responds to the light intensity by changing the reverse current in the order of microampere. Even though the quality of the device is not sufficiently high but a possible application for this device is photonic applications, such as a photodetector.
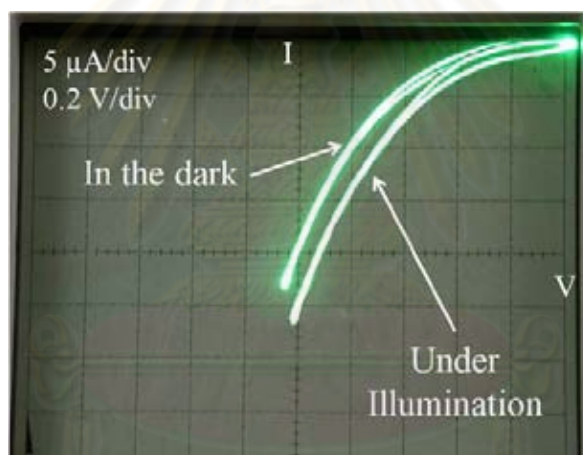
Fig 4.19 I-V characteristic in the dark and under illumination of the sample in Fig 4.17
with GaAs thickness of 500 nm.

4.4.3 Experimental Result on InAs-QD p-n Junction
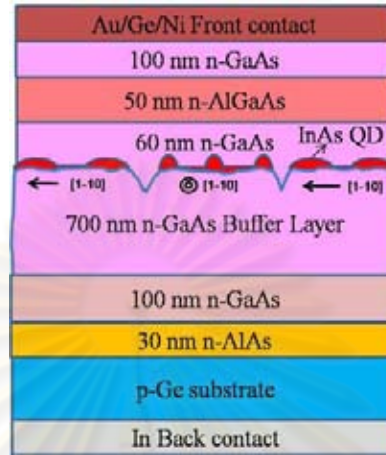
Fig 4.20 Schematic structure of InAs-QD p-n Junction.

We have grown InAs QDs on n-GaAs buffer layer to charactize its electrical property. The schematic structure of InAs QD p-n junction is illustrated in Fig 4.20. The APDs and dislocations still exist. In this sample, n-AlAs blocking layer and 100 nm-GaAs layer were grown by MEE technique at 350°C with AlAs and GaAs growth rate of 0.1 ML/s. GaAs buffer layer was also grown by the MEE technique at this temperature with GaAs growth rate of 0.5 ML/s. The substrate temperature was then increased to 500°C in order to grow InAs QDs at this temperature. After finishing this process, the substrate temperature was then increased to 520°C and InAs QDs were capped by n-GaAs, n-Al$_{0.17}$Ga$_{0.83}$As, and n-GaAs with thickness of 60, 50, and 100 nm, respectively. I-V characteristic of InAs QD p-n junction is shown in Fig 4.21. I-V curve exhibits the p-n junction diode with cut-in voltage of 0.7 V. However, the junction quality is quite low as we can see from the high leakage current. Thus, the junction quality must be improved to provide better electrical performance.
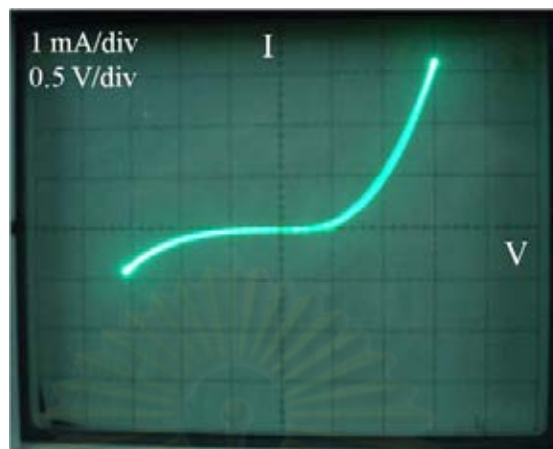
Fig 4.21 I-V characteristic of InAs QD p-n junction.

4.5 Spectral Response Characteristics of GaAs on AlAs/Ge substrate

The structure in Fig 4.17 with GaAs thickness of 500 nm has been characterized and described by spectral response. The spectral response measuremeant setup is illustrated in Fig 3.14. Spectral response characteristic of GaAs on AlAs/Ge substrate is shown in Fig 4.22. At short wavelengths below 550 nm the sample absorbs most of the incident light and its response is very low. However, the sample responds to wavelength ranging from 500 nm to 900 nm. More experimental results are needed to explain its spectral response behavior.
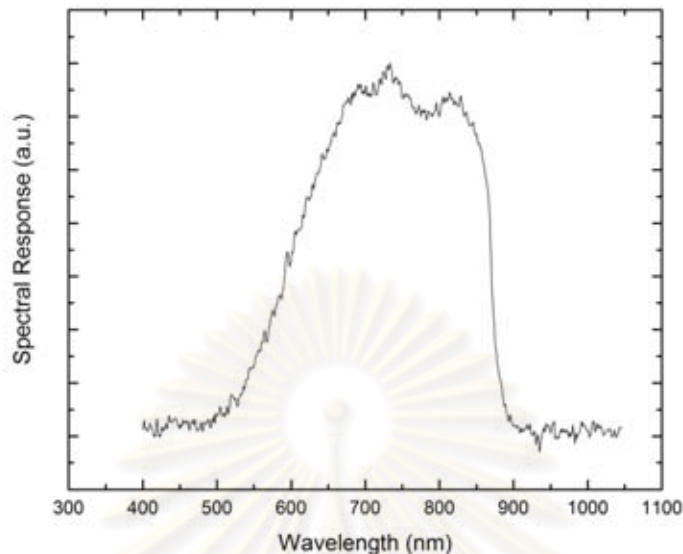
Fig 4.22 Spectral response characteristics of GaAs on AlAs/Ge substrate.

4.6 Photoluminescence (PL) Results and Discussions

PL results of GaAs grown on AlAs/Ge substrate are shown in Fig 4.23 (a) and (b) with different measurement conditions. Fig 4.23 (a) shows the PL spectra of 500-nm GaAs grown on AlAs/Ge substrate with varying excitation laser power. From this figure, there is no spectral shift but only decreasing spectral peak intensity at 1.15 and 1.35 eV. All spectra of GaAs on AlAs/Ge show three different structures, one narrow band-to-band (B2B) at an energy of 1.5 eV, a broad inner-band-gap (IB) structure at an energy of ~1.1 eV as also observed by Brammertz et al. [60] and unidentified structure at an energy of ~1.3 eV. Small strain in the AlAs layer causes strain in GaAs buffer layer leading to the B2B structure which leads to the separation into a light-hole and a heavy-hole peak. The IB structure observed from PL spectra consists of two Gaussian peaks with energies of 1.04 and 1.15 eV as shown in Fig 4.24. This result is consistent with Brammertz's result except for the peak at ~1.35 eV. The peak at 1.04 eV is due to a Ge_{Ga}-Ge_{As} complex, whereas the peak at 1.17 eV is attributed to the Ge_{Ga}-V_{Ga} complex [61]. One reasonable explanation from this result is that AlAs compound semiconductor is an

ineffectively blocking layer if Ge substrate is oriented. APDs could be formed inside the AlAs structure, therefore Ge, Ga, As or even Al atoms can diffuse across AlAs/Ge interface and reach GaAs buffer layer leading to Ge-based complexes formed within GaAs buffer layer. More experimental results are needed to explain this phenomena and to identify the spectral peak at ~1.35 eV. From Fig 4.23 (b), the PL peak is slightly red-shifted at high temperatures. This is reasonable because when the sample temperature is increased, existing splitting bands can merge, as predicted by Varshni equation [62]. PL peak energy and FWHM of 4 curves, corresponding to Fig 4.24, with various temperature and laser power are shown on Table 4.1 and 4.2.

Fig 4.25 shows the PL result of InAs QDs grown on 300 nm GaAs buffer layer with laser power of ~20 mW at 20 K. We cannot observe any emission peaks of InAs QDs in this PL spectrum. This PL result is due to the defects in GaAs buffer layer. Once electron in the QDs have been excited, the distribution of electron is no longer in equilibrium, and they eventually decay into lower states but, prior to reaching the appropriate lower states, they are trapped by APB which is formed closely to QDs alignment resulting in non-radiative recombination process. Since APBs comprise the planes of wrong nearest neighbor bonds where Ga atoms and As atoms reverse their positions crystallographically during the growth of polar material on the non-polar substrate, they are electrically active defects known to cause carrier scattering and non-radiative recombination [59, 37]. Quantum dot quality can be improved by optimizing growth conditions, such as InAs coverage and QDs growth temperature, which consequently affect the improvement of PL results.
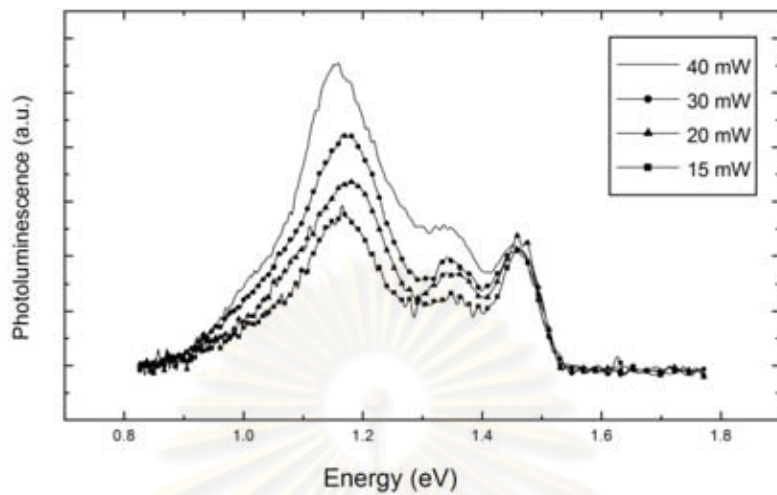
(a)
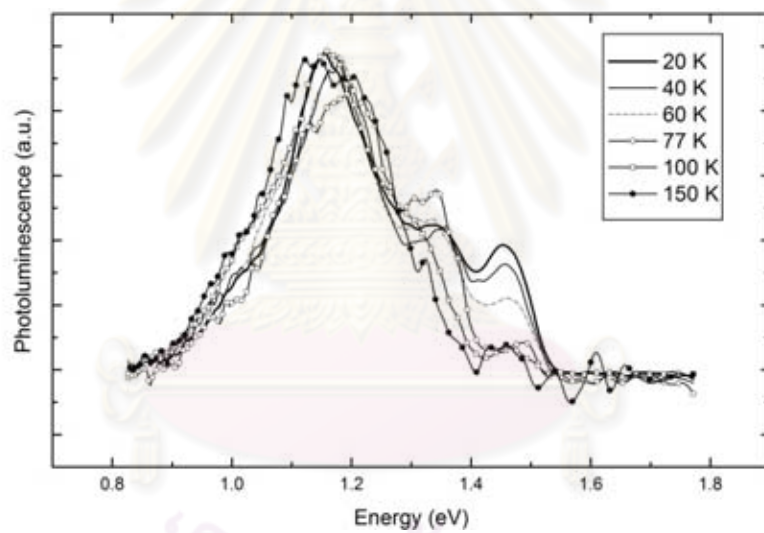
(b)

Fig 4.23 PL spectra of 500 nm GaAs grown on AlAs/Ge substrate varying (a) laser power and (b) substrate temperature.
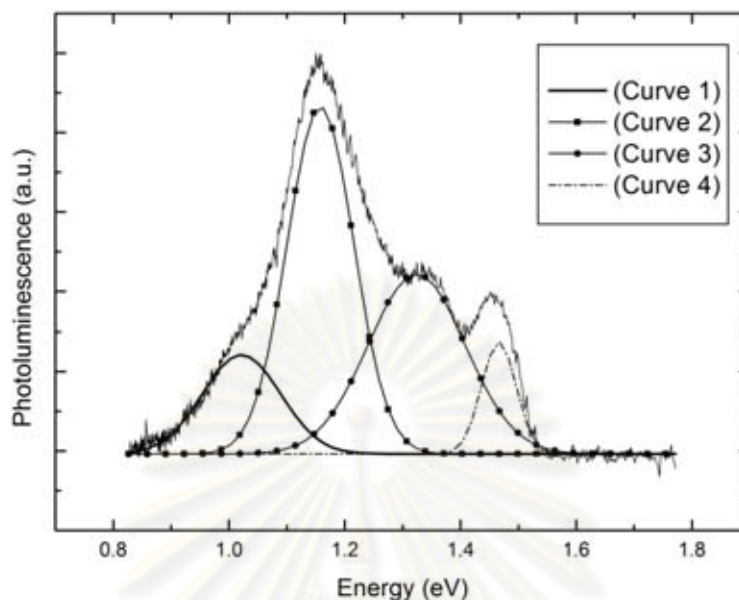
Fig 4.24 Two Gaussian peaks of IB structure with energy of 1.04 (curve 1) and 1.15 eV
(curve 2) at 20 K and 40 mW. Unidentified structure and B2B are at the energy
of ~1.3 (curve 3) and 1.47 eV (curve 4), respectively.

Table 4.1 PL peak energy and FWHM of 4 curves, corresponding to Fig 4.24 at various
temperatures with 40 mW laser power.

Measured values		Temperature (Kelvin), 40 mW					
		20	40	60	77	100	150
PL Peak energy (eV)	Curve 1	1.022	1.059	1.067	1.058	1.060	0.989
	Curve 2	1.158	1.188	1.186	1.195	1.171	1.099
	Curve 3	1.324	1.352	1.340	1.349	1.298	1.207
	Curve 4	1.466	1.464	1.462	1.475	1.467	-
FWHM (meV)	Curve 1	159.21	223.15	218.64	241.70	194.07	128.88
	Curve 2	135.39	146.68	147.68	202.84	124.86	123.36
	Curve 3	198.83	116.06	105.56	77.73	194.07	184.79
	Curve 4	71.45	77.73	85.75	76.72	57.17	-

Table 4.2 PL peak energy and FWHM of 4 curves, corresponding to Fig 4.24 with various laser powers at 20 K.

Measured values		Laser power (mW), 20 K			
		15	20	30	40
PL Peak energy (eV)	Curve 1	1.137	1.121	1.077	1.022
	Curve 2	1.170	1.186	1.186	1.158
	Curve 3	1.358	1.358	1.354	1.324
	Curve 4	1.465	1.464	1.462	1.466
FWHM (meV)	Curve 1	261.57	262.01	227.66	159.21
	Curve 2	107.06	133.39	138.65	135.39
	Curve 3	134.64	102.30	119.60	198.83
	Curve 4	70.70	72.46	75.72	71.45
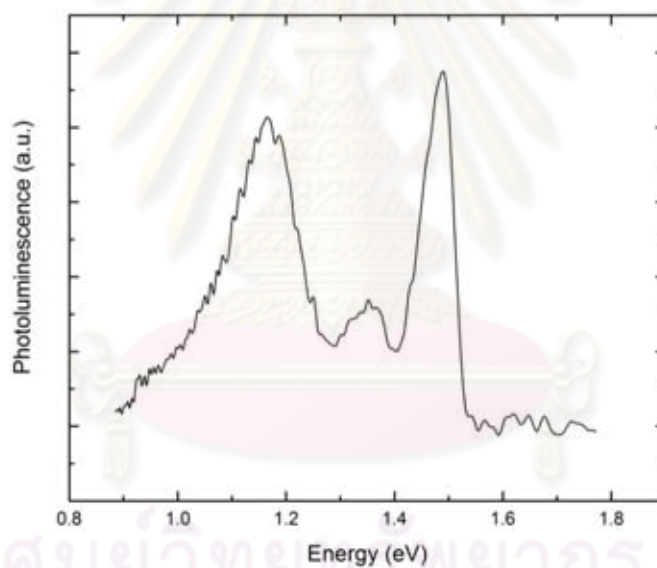
Fig 4.25 PL result of InAs QDs grown on 300 nm GaAs buffer layer with laser power of ~20 mW at 20 K.

CHAPTER V

CONCLUSIONS

This work presents the MBE growth of GaAs on Ge substrates. By varying the thickness of GaAs, different domain sizes of GaAs can be obtained. InAs QDs, grown on APD-GaAs is also studied.

Firstly, a brief overview on the properties of low-dimensional nanostructures was given. As an example of the QD fabrication in lattice-mismatched system, self-assembled growth in the Stranski-Krastanow mode was briefly reviewed. Details of migration-enhanced epitaxy that was the technique for growing high quality layer were described. From material considerations, the information of the material system including InAs/GaAs was discussed. The explanation of anti-phase domains, resulting from polar/non-polar property, was revealed. The properties of p-n junction were shortly discussed.

In situ RHEED method was used to determine the growth rates and monitor surface structure during the growth of GaAs, AlAs and nanostructures on Ge substrates. The surface morphology and structural properties of the samples with self-assembled InAs quantum dots were investigated by *ex situ* atomic force microscope (AFM) and photoluminescence (PL) measurement at various temperatures and power excitation. The crystal quality and the defects in the samples were investigated by X-ray diffraction (XRD) method and transmission electron microscopy (TEM). The basic of spectral response property was also shortly described.

The fabrication of GaAs on Ge substartes was done by migration-enhanced epitaxy (MEE) technique using solid source molecular beam epitaxy (MBE). The growth processes, consists of 7 steps : 1) pre-heated process, 2) de-oxidation (removing oxide from substrate surface), 3) growth of AlAs interfacial layer by MEE technique, 4) growth of GaAs by MEE technique, 5) a two step GaAs nucleation process, 6) self-assembled InAs QDs nucleation process, and 7) the capping process for PL measurement.

The GaAs thickness was varied in order to investigate the effects on the GaAs domain size. GaAs domain size varies with GaAs thickness. The XRD and TEM results

indicate the crystal imperfections of GaAs grown on Ge substrates. However, most of stacking faults and dislocations disappear before reaching the GaAs surface. The GaAs/p-Ge schottky devices and p-n junction devices are fabricated. From I-V characteristics, some samples, responding to the light intensity, exhibit the photodetector characteristic. According to the spectral response results, GaAs on AlAs/Ge substrate responds to the light intensity having wavelength ranging from 500 nm to 900 nm. PL results of GaAs grown on AlAs/Ge substrate show three different structures consisting of one narrow band-to-band (B2B) at an energy of 1.5 eV, a broad inner-band-gap (IB) structure at an energy of ~1.1 eV, and unidentified structure at an energy of ~1.3 eV. More experimental results are needed to identify the spectral peak at 1.3 eV.

For nanostructures, self-assembled InAs QDs are grown on Ge substrates using a GaAs buffer layer and AlAs interfacial layer. The Effect of GaAs thickness on size, height, and density of InAs QDs on Ge substrates are investigated. Anisotropic property affects the quantum dot shape. InAs QDs grown on APDs-GaAs buffer layer align in specific crystallographic direction for each domain. From I-V characteristics of InAs QDs grown on GaAs/Ge substrates, the sample exhibits the p-n junction diode. The junction quality must be improved to provide better electrical performance. In this work, PL result does not show any emission peaks from InAs QDs grown on Ge substrates.

REFERENCES

[1] Ringel, S.A., Sieg, R.M., Ting, S.M., and Fitzgerald, E.A. <u>26th PVSC</u>, Anaheim, CA, Sept. 30- Oct. 3, 1997

[2] Chenh, K.Y. <u>IEEE Proc.</u>, vol.85, no.11, pp.1694-1714, 1997.

[3] Bertness, K.A., Friedman, D.J., Kurtz, Sarah R., Kibbler, A.E., Kramer, C., and Olson, J.M. <u>IEEE AES Systems Magazine</u>, vol. 9, issue. 12, pp. 12-17, Dec 1994.

[4] Loper, P., et al. <u>Silicon quantum dot superstructures for all-silicon tandem solar cells: Electrical and optical characterization</u> [Online]. (2009). Available from: www.quantsol.org/pub/pub09_31.pdf [2010, November 28]

[5] Green, M.A., et al. <u>23rd European Photovoltaic Solar Energy Conference and Exhibition</u>. pp.1-4, Valencia, Spain, 2008.

[6] Stan, M.A., et al. <u>29th IEEE Photovolt. Specialists Conf</u>. pp.816-819, 2002.

[7] Kurtz, S.R., and Friedman, D.J. <u>Presented at the National Center for Photovoltaics Program Review Meeting</u>. Denver, Colorado, Sept. 8-11, 1998.

[8] Kamath, K., Bhattacharya, P., Sosnowski, T., Norris, T., and Phillips, J. <u>Electron. Lett</u>. 32 (1996) : 1374.

[9] Huffaker, D. L., Park, G., Zou, Z., Shchekin, O.B., and Deppe, D.G. <u>Appl. Phys. Lett</u>. 73 (1998) : 2564.

[10] Kovsh, A. R., et al. <u>Electron. Lett</u>. 35 (1999) : 1161.

[11] Sugawara, M., Hatori, N., Akiyama, T., Nakata, Y., and Ishikawa, H. <u>Jpn. J. Appl. Phys</u>. 40 Part 2 (2001) : 488.

[12] Borri, P., et al. <u>Appl. Phys. Lett</u>. 79 (2001) : 2633.

[13] Berryman, K.W., Lyon, S.A., and Segev, M. <u>Appl. Phys. Lett</u>. 70 (1997) : 1861.

[14] Philips, J., Bhattacharya, P., Kennerly, S.W., Beekman, D.W., and Dutta, M. <u>IEEE J. Quantum Electron</u>. 35 (1999) : 936.

[15] Sangu, S., Kobayashi, K., Shojiguchi, A., and Ohtsu, M. <u>Phys. Rev. B</u> 69 (2004) : 115334.

[16] Kiraz, A., Atature, M., and Imamoglu, A. <u>Phys. Rev. A</u> 69 (2004) : 032305.

[17] Dhawan, T., et al. <u>Nanoscale Res Lett</u> 5 (2010) : 31-37.

[18] Knuuttila, L., Kainu, K., Sopanen, M., and Lipsanen, H. <u>J. Mater. Sci. Mater. Electron</u>. 14 (2003) : 349.

[19] Chia, C.K., et al. <u>Appl. Phys. Lett</u>. 92 (2008) : 141905.

[20] Bimberg, D., Grundmann, M., and Ledentsov, N.N. <u>Quantum dot heterostructures</u>. Chichester, Wiley, 1999.

[21] Sugawara, M. Theoretical Bases of the Optical Properties of Semiconductor Quantum Nano-Structures. In M. Sugawara (ed.), <u>Semiconductors and semimetals vol.60: Self-Assembled InGaAs/GaAs Quantum Dots</u>. pp.1-116. San Diego : Academic Press, 1999.

[22] Bastard, G., and Brum, J.A. <u>Electronic states in semiconductor heterostructures</u>. <u>IEEE J. Quantum Electron</u>. 22 (1986) : 1625-1644.

[23] Arakawa, Y. and Sakaki, H. Multidimensional quantum well laser and temperature dependence of its threshold current. <u>Appl. Phys. Lett</u>. 40 (1982) : 939.

[24] Asada, M., Miyamoto, Y., and Suematsu, Y. Gain and the threshold of three-dimensional quantum-box lasers. <u>IEEE J. Quantum Electron</u>. 22 (1986) : 1915-1921.

[25] Zhukov, A.E., et al. 3.5 W continuous wave operation from quantum dot laser. <u>Materials Science and Engineering B</u> 74 (2000) : 70-74.

[26] Herman, M.A., and Sitter, H. <u>Molecular beam epitaxy—fundamentals and current status</u>. Springer-Verlag Berlin-Heidelberg-New York-London-Paris-Tokyo, 1989.

[27] Seifert, W., et al. In-situ growth of quantum dot structures by the Stranski-Krastanow growth mode. <u>Crystal Growth and Characterization</u> 33 (1996) : 423-471.

[28] O'Reilly, E.P. Valence band engineering in strained-layer structures. <u>Semiconductors Science and Technology</u> 4 (1989) : 121-137.

[29] Horikoshi, Y., Kawashima, M., and Yamaguchi, H. <u>Jpn. J. Appl. Phys</u>. 25 (1986) : L868.

[30] Horikoshi, Y., Kawashima, M., and Yamaguchi, H. <u>Jpn. J. Appl. Phys</u>. 27 (1988) : 169.

[31] Horikoshi, Y., Yamagushi, H., Briones, F., and Kawashima, M. <u>J. Cryst. Growth</u> 105 (1990) : 326.

[32] Homma, Y., Yamaguchi, H., and Horikoshi, Y. <u>Appl. Phys. Lett</u>. 68 (1996) : 63-65.

[33] Nishinaga, T., and Cho, K.I. <u>Jpn. J. Appl Phys</u>. 27 (1988) : L12.

[34] Kobayashi, N., and Horikoshi, Y. <u>Jpn J. Appl. Phys</u>. 28 (1989) : L1880.

[35] Sudersena Rao, T., Nozawa, K., and Horikoshi, Y., <u>Jpn. J. Appl. Phys</u>. 30 (1991) : U47.

[36] Kroemer, H. <u>J. Cryst. Growth</u> 81 (1987) : 193.

[37] Noge, H., Kano, H., Hashimoto, M., and Igarashi, I. <u>J. Appl. Phys</u>. 64 (1988) : 2246.

[38] Holt, D.B., et al. <u>Microscopy of Semiconducting Materials 1995: Proceedings of the Institute of Physics Conference</u>. Oxford University, 20–23 March 1995.

[39] Griffith, J.E., and Kochanski, G.P. <u>Crit. Rev. Solid State Mater. Sci</u>. 16 (1990) : 255.

[40] Griffith, J.E., Kubby, J.A., Wierenga, P.E., Becker, R.S., and Vickers, J.S. <u>J. Vac. Sci. Technol. A</u> 6 (1998) : 493.

[41] Yasuda, T., Mantese, L., Rossow, U., and Aspnes, D.E. <u>Phys. Rev. Lett</u>. 74 (1995) : 3431.

[42] Pukite, P.R., and Cohen, P.I. <u>J. Cryst. Growth</u> 81 (1987) : 214.

[43] Pukite, P.R., and Cohen, P.I. <u>Appl. Phys. Lett</u>. 50 (1987) : 1739.

[44] Becker, R.S., Klitsner, T., and Vickers, J.S. <u>J. Microsc</u>. 152 (1988) : 157.

[45] Ohno, T.R., and Williams, E.D. <u>Jpn. J. Appl. Phys</u>., Part 2 28 (1989) : L2061.

[46] Bartels, W. Characterization of thin layers on perfect crystals with a multipurpose high resolution x-ray diffractometer. <u>J. Vac. Sci. Technol. B</u> 1 (1983) : 338–345.

[47] Fitzgerald, E.A., Kuo, J.M., Xie, Y.H., and Silverman, P.J. Necessity of Ga prelayers in GaAs/Ge growth using gas-source molecular beam epitaxy. <u>Appl. Phys. Lett</u>. 64 (1994) : 733-735.

[48] Strite, S., et al. GaAs/Ge/GaAs heterostructures by molecular beam epitaxy. <u>J. Vac. Sci. Technol. B</u> 8 (1990) : 1131- 1140.

[49] Ting, S.M., Fitzgerald, E.A., Sieg, R.M., and Ringel, S.A. Range of defect morphologies on GaAs grown on offcut (001) Ge substrates. <u>J. Electron. Mater</u>. 27, Issue 5, May 1, 1998.

[50] Fang, S.F., et al. Gallium arsenide and other compound semiconductors on silicon. <u>J. Appl. Phys</u>. 68 (1990) : R31-R58.

[51] Rosner, S.J., Koch, S.M., Laderman, S., and Harris, J.S. <u>Proc. MRS 1986 Spring meeting</u> 67 (1986) : 77.

[52] Biegeisen, D.K., Ponce, F.A., Smith, A.J., and Tramontana, J.C. <u>Proc. 1986 Spring MRS Meeting</u> 67 (1986) : 45.

[53] Rosner, S.J., Koch, S.M., and Harris, Jr., J. Proc. 1987 Spring MRS Meeting 91 (1987) : 155.

[54] Biegelsen, D.K., Ponce, F.A., Smith, A.J., and Tramontana, J.C. Proc. 1986 Spring MRS Meeting 67 (1986) : 45.

[55] Zhou, J.M., Guo, L.W., Cui, Q., Peng, C.S., and Huang, Q. Conversion of step configuration induced by strain in $Si_{l-x}Ge_x$ layers deposited on vicinal Si (001) surface. Appl. Phys. Lett. 68 (1996) : 628-630.

[56] Chand, N., Klem, J., Henderson, T., and Morkoc, H. Diffusion of As and Ge during Growth of GaAs on Ge substrate by Molecular Beam Epitaxy: Its Effect on the Device Electrical Characteristics. J. Appl. Phys. 59, no.10 (1986).

[57] Chia, C.K., et al. Effects of AlAs interfacial layer on material and optical properties of GaAs/Ge(100) epitaxy. Appl. Phys. Lett. 92 (2008) : 141905.

[58] Suraprapapich, S., Kanjanachuchai, S., Thainoi, S., and Panyakeow, S. Microelectron. Eng. 78–79 (2005) : 349–352.

[59] Ting, S.M., and Fitzgerald, E.A. J. Appl. Phys. 87 (2000) : 2618.

[60] Brammertz, G., et al. Appl. Phys. 99 (2006) : 093514.

[61] Hudait, M.K., Modak, P., Hardikar, S., and Krupanidhi, S.B. J. Appl. Phys. 83 (1998) : 4454.

[62] O'Donnell, K.P., and Chen, X. Appl. Phys. Lett. 58 (1991) : 2924.

Appendix

LIST OF PUBLICATIONS

1. Tantiweerasophon, W., Suraprapapich, S., Nuntawong, N., Thainoi, S., and Panyakeow, S. <u>Molecular Beam Epitaxial Growth of GaAs on Ge substrates and their photonic device applications</u>. The 31st Electrical Engineering Conference (EECON-31), Royalhills Golf Resort and Spa, Nakornnayok, pp.1197-1200, 29-31 October, 2008.

2. Tantiweerasophon, W., Thainoi, S., Changmuang, P., Kanjanachuchai, S., Rattanathammaphan, S., and Panyakeow, S. <u>Self-assembled InAs quantum dots on anti-phase domains of GaAs on Ge substrates</u>. Journal of Crystal Growth, (2011) (accepted, in press).

LIST OF PRESENTATIONS

1. Tantiweerasophon, W., Thainoi, S., Changmuang, P., Kanjanachuchai, S., Rattanathammaphan, S., and Panyakeow, S. <u>Self-assembled InAs quantum dots on anti-phase domains of GaAs on Ge substrates</u>. 16th International Conference on Molecular Beam Epitaxy (MBE 2010), Berlin, Germany, 22-27 August, 2010.

VITAE

Wichit Tantiweerasophon was born in Samutprakarn, Thailand on August 18, 1984. He graduated from Triamudomsuksa Pattanakarn in March 2003. In June 2003, he entered Chulalongkorn University and received the Bachelor of Engineering in Electrical Engineering in April 2007. In June 2007, he was further his study as a master student.